Research on Harmonic State-Space Modeling and Calculation Analysis of Low-Switching-Frequency Grid-Connected Inverter Considering the Impact of Digitization

Yuxi Cai, *Student Member, IEEE*, Yingjie He, *Senior Member, IEEE*, Haixiao Zhang, *Student Member, IEEE*, Hongwei Zhou, *Member, IEEE*, and Jinjun Liu, *Fellow, IEEE*

***Abstract*—Under low-switching-frequency condition, there is harmonic coupling in grid-connected inverter. The harmonic state-space (HSS) modeling method is an effective means to analyze the output harmonic characteristics of inverter. When the switching frequency is low, the sampling/holding and control delay make the update of pulsewidth modulation pulses more untimely, which will have a non-negligible impact on system output. However, the current relevant research fails to take these factors into account in the HSS model. In addition, the existing work fails to thoroughly study the calculation and analysis methods of HSS model, and the relevant work is insufficient. Based on this, this article studies the closed-loop HSS model and its calculation and analysis methods of three-level grid-connected inverter considering the digitization impact. First, according to the different calculation and analysis methods of the HSS model of the grid-connected inverter, the methods considering the digitization impact are proposed, respectively. Second, according to the proposed method, the harmonic characteristics of low-switching-frequency grid-connected inverter are analyzed, and the necessity of considering the digitization impact is explained. Finally, the effectiveness and accuracy of the proposed HSS-model calculation and analysis methods considering the digitization impact are verified by simulation and experiment.**

***Index Terms*—Control delay, digitization, harmonic characteristic, harmonic state-space (HSS), *LCL* grid-connected inverter (GCI), low switching frequency (LSF).**

Manuscript received 28 April 2022; revised 7 July 2022; accepted 19 August 2022. Date of publication 25 August 2022; date of current version 10 October 2022. This work was supported in part by the National Natural Science Foundation of China under Grant 51777158, in part by the Intelligent Electric Power Grid Key Laboratory Open Fund of Sichuan Province under Grant 2022-IEPGKLSP-KFYB03, and in part by Basic Science Research Fund in Xi'an Jiaotong University under Grant 11913222000010. Recommended for publication by Associate Editor G.-S. Seo. *(Corresponding author: Yingjie He.)*

Yuxi Cai, Haixiao Zhang, and Jinjun Liu are with the School of Electrical Engineering, Xi'an Jiaotong University, Xi'an 710049, China (e-mail: 412561351@163.com; 291645746@qq.com; jjliu@mail.xjtu.edu.cn).

Yingjie He is with the School of Electrical Engineering, Xi'an Jiaotong University, Xi'an 710049, China, and also with the Intelligent Electric Power Grid Key Laboratory of Sichuan Province, Sichuan University, Chengdu 610065, China (e-mail: hyj202411@sina.com).

Hongwei Zhou is with the School of Electrical Engineering, Xi'an Jiaotong University, Xi'an 710049, China, and also with the TBEA Xi'an Electric Technology Company, Ltd., Xi'an 710119, China (e-mail: zhouhongwei@stu.xjtu.edu.cn).

Color versions of one or more figures in this article are available at https://doi.org/10.1109/TPEL.2022.3201626.

Digital Object Identifier 10.1109/TPEL.2022.3201626

NOMENCLATURE

GCI	Grid-connected inverter.
TL	Three-level.
NPC	Neutral point clamped.
LSF	Low switching frequency.
SSAV	State-space averaging.
GA	Generalized averaging.
HTF	Harmonic transfer function.
GCF	Grid-side current feedback.
CCF	Capacitor current feedback.
AD	Active damping.
S/H	Sampling/holding.
SM	State matrix.
IM/OM/IOM	Input/output/input–output matrix.
CS	Control system.
NU	Nonideal unit (generated by digital control).
AR	After reconstruction.
x	Midpoint of three-phase bridge arm, $x =$ a, b, c.
u_{gx}	Three-phase grid voltages.
i_{cx}	Three-phase capacitor currents.
i_{ix}	Three-phase inverter-side currents.
i_{gx}/i_{gx}^*	Three-phase grid-side currents/references.
s_x	Three-phase switching functions.
f_s/T_s	Sampling frequency/period.
$f_{\rm sw}/T_{\rm sw}$	Switching frequency/period.

Time-Domain Symbol

x_{im}, u_{im}, y_{im}	State variables, inputs, and outputs of plant.
A_i, B_i, C_i	SM, IM, and OM of plant.
x_{ic}, u_{ic}, y_{ic}	State variables, inputs, and outputs of CS.
E_i, F_i, G_i, H_i	SM, IM, OM, and IOM of CS.
x_{id}, u_{id}, y_{id}	State variables, inputs, and outputs of NU.
I_i, J_i, K_i, L_i	SM, IM, OM, and IOM of NU.
x_m, u_m, y_m	State variables, inputs, and outputs of plant AR.
A_s, B_s, C_s	SM, IM, and OM of plant AR.
x_c, u_c, y_c	State variables, inputs, and outputs of CS AR.
E_s, F_s, G_s, H_s	SM, IM, OM, and IOM of CS AR.
x_d, u_d, y_d	State variables, inputs, and outputs of NU AR.
I_s, J_s, K_s, L_s	SM, IM, OM, and IOM of NU AR.

x_p, u_p, y_p	State variables, inputs, and outputs of whole system.
A_p, B_p, C_p	SM, IM, and OM of whole system.

Frequency-Domain Symbol

X_{imh}, U_{imh}, Y_{imh}	State variables, inputs, and outputs of plant.
$\mathcal{A}_{ih}, \mathcal{B}_{ih}, C_{ih}$	SM, IM and OM of plant.
X_{ich}, U_{ich}, Y_{ich}	State variables, inputs, and outputs of CS.
$E_{ih}, \mathcal{F}_{ih}, \mathcal{G}_{ih}, \mathcal{H}_{ih}$	SM, IM, OM and IOM of CS.
X_h, U_h, Y_h	State variables, inputs, and outputs of whole system.
$\mathcal{A}_h, \mathcal{B}_h, C_h$	SM, IM and OM of whole system.
N_m, N_c, N_h	Modulation frequency matrix.

I. Introduction

GRID-CONNECTED inverter (GCI) is the interface device between new energy power generation system and utility grid, its characteristic analysis has always been a research hotspot [1], [2]. At present, the power of high-power GCI is generally several hundred kilowatts to several megawatts. The three-level (TL) neutral-point-clamped (NPC) topology and *LCL*-type filter are often used, and the switching frequency is between 2 and 3.5 kHz [3], [4]. Under low-switching-frequency (LSF) condition, the control loop, resonant peak of the *LCL* filter and sideband harmonics generated by modulation are coupled in mid-frequency band, which makes it difficult to calculate and analyze the harmonic content and harmonic characteristics of the inverter output current by traditional modeling methods. Therefore, it is necessary to establish an accurate mathematical model for LSF *LCL* GCI to complete the above works.

At present, the models of *LCL* GCI are mainly divided into the following two categories: single-frequency model and multifrequency model. The single-frequency model refers to the mathematical description of the relationship between the input and output components of the same frequency in the system. The state-space averaging (SSAV) model is a typical single-frequency model. It uses the switching-period average operator to convert the discrete system model into a continuous model, and then obtains the linear time-invariant (LTI) model of the system through the linearization method [5], [6], [7], [8], [9]. The SSAV modeling method is easy. However, because it only describes the relationship between the input and output components of the same frequency in the system, it cannot reflect the coupling between the input of a certain frequency and the output of other frequencies. The multifrequency model is a mathematical description of the relationship between the input and output components of multiple frequencies in the system. It mainly includes the generalized averaging (GA) model (i.e., dynamic phasor) and harmonic state-space (HSS) model. Among them, the GA model is an improvement of the SSAV model. The harmonic term $e^{-jk\omega 1T}$ is added to the switching-period average operator to obtain the generalized switching-period average operator [10], [11], [12]. This new operator and linearization method are used to deal with the discrete nonlinear system, and then the GA model of the system is obtained. The GA model is also widely used in power electronics. For example, it is used for the modeling of the inverter-based microgrid system under asymmetric fault [13], the modeling of GCI in the case of unintentional island [14], and the accurate modeling of double active bridges [15]. Because the GA model takes into account multiple dominant frequencies of the system, it has higher accuracy than SSAV model. However, for LSF *LCL* GCI, it is difficult to obtain its dominant frequencies due to harmonic coupling and complex harmonic characteristics, therefore, its GA model is difficult to accurately reflect its output harmonic characteristics. The other multifrequency model is an HSS model. The biggest difference between it and the first two modeling methods is, the first two modeling methods are linearized at the steady-state working point, while HSS model is linearized on the operating trajectory, so it is a linear time-periodic (LTP) model. HSS characterizes the input and output signals in the form of finite harmonic components, respectively, and converts the periodic variables in the time domain into constants in the frequency domain through Fourier series, which is equivalent to building a multiple-input multiple-output LTI model in the frequency domain. So HSS model can reflect the coupling between the input and output components of each frequency [16], [17], [18]. At present, the application of the HSS model in the power electronic converter has been reported, such as the research on accurate impedance modeling of modular multilevel converters based on HSS [19], [20], [21], the research on HSS modeling and stability of the dc–dc system [22], the research on HSS modeling and harmonic stability of the *LCL* inverter system [23], [24], [25], [26], [27], [28], [29], [30], [31], [32]. However, there are still some deficiencies in the research on HSS modeling and analysis of LSF *LCL* GCI. The following will summarize the current relevant research.

In [23] and [24], the HSS model of *LCL* GCI based on dc side voltage + output current control was established. The two literatures analyzed the harmonic relationship between dc-side voltage and ac-side current and between grid voltage and output current of GCI. Kwon et al. [25] constructed the open-loop HSS model of *LCL* GCI, and explained the influence of modulation on inverter output through bode diagram of harmonic transfer function (HTF). In [26], the influence of PLL on the system was taken into account, the closed-loop HSS model of *LCL* GCI was established, and the stability range of the system was estimated. Chen et al. [27] established the closed-loop HSS model of virtual synchronous generator, and analyzed the system stability through eigenvalues. Kwon et al. [28] established the HSS model for the back-to-back system, and analyzed its coupling relationship between ac and dc sides. Taking five *LCL* GCIs as example, the HSS model of the multi-inverter parallel system was built in [29], and the influence of each-phase grid voltage harmonic on the output current of each inverter was analyzed. At the application level of HSS model, HSS modeling was used to address the nonlinearity issue of the static var compensator coupling hybrid active power filter, which enabled the linear-matrix-inequality

based H_∞ optimal control techniques [30]. Sun et al. [31] completed the harmonic calculation of output current through the HSS model of GCI, to guide the design of control parameters. In addition, Zhang et al. [32] also constructed the HSS model of GCI, which was used for cyber-attack detection of inner current controller in photovoltaic inverter. In the abovementioned works, there are the following deficiencies in HSS modeling and analysis. First, the existing work fails to thoroughly study the modeling process and calculation and analysis methods of HSS according to different application backgrounds. Second, under LSF condition, the nonideal factors such as sampling/holding (S/H) and control delay caused by digital control have a significant impact on system output, which cannot be ignored. However, the existing HSS model fails to include the above parts, so the accuracy of the HSS model of *LCL* GCI needs to be further improved.

Taking the *LCL* TL-NPC GCI commonly used in photovoltaic system as the research object, the accurate HSS model considering the digitization impact and its calculation and analysis methods are studied. First, the harmonic coupling phenomenon and the necessity of considering the impact of digitization are explained. Second, for the two calculation and analysis methods of closed-loop HSS model of GCI (i.e., iterative calculation method and frequency-domain analysis method), the methods considering the nonideal factors, such as S/H and control delay are proposed, respectively. Finally, the harmonic characteristics of LSF GCI are analysed based on the proposed model and method, and the effectiveness and accuracy of the calculation and analysis methods of HSS model considering digitization proposed in this article are verified by simulation and experiment.

The contributions of this article are as follows. Two calculation and analysis methods of HSS model are studied in detail, namely iterative calculation method and frequency-domain analysis method. Meanwhile, for different calculation and analysis methods of HSS model, the methods considering the impact of digitization are proposed, respectively.

1) An improved iterative-calculation-method of HSS model considering the digitization impact and switching frequency is proposed in this article. This method effectively improves the calculation accuracy of inverter output harmonics without increasing the complexity of the model.
2) A complete closed-loop HSS model of inverter including S/H and control delay is established, which improves the modeling process of HSS, facilitates the frequency-domain analysis, and improves the accuracy of harmonic characteristic analysis of LSF *LCL* GCI.

The rest this article is organized as follows. Section II introduces the structure of GCI, and explains the harmonic coupling phenomenon and the necessity of considering the digitization impact. Section III is an overview of HSS model. Section IV first introduces the basic HSS model of GCI, then studies two calculation and analysis methods of HSS model, and proposes the methods considering the digitization impact, respectively. Sections V and VI are harmonic characteristic analysis and simulation and experimental verification. Finally, Section VII concludes this article.

II. Description of GCI System and Relevant Problems

A. GCI System

The *LCL* TL-NPC GCI system based on grid-side-current-feedback (GCF) PI + capacitor-current-feedback (CCF) active damping (AD) is shown in Fig. 1. Use x to represent the midpoint of three-phase bridge arm, i.e., x = a, b, c. C_1 and C_2 are the dc side supporting capacitors, L_1, L_2, and C are the inverter-side filter inductor, grid-side filter inductor, and filter capacitor, respectively. $U_{\rm dc}$ is the dc-side voltage, $u_{\rm gx}$, $i_{\rm cx}$, $i_{\rm ix}$, and $\rm i_{gx}$ are three-phase grid voltage, capacitor current, inverter-side current, and grid-side current, respectively.

B. Harmonic Coupling Phenomenon and HSS Modeling Necessity

The output current spectrum of GCI can be divided into three-frequency bands, namely low-frequency band, mid-frequency band, and high-frequency band. Low-frequency band refers to the area within the control bandwidth f_b, which is the main working range of closed-loop control. High-frequency band refers to the area above $f_{\rm sw}/2$, which mainly includes sideband harmonics generated by modulation. Wherein, $f_{\rm sw}$ is switching frequency. The main function of filter is to filter out these harmonics. The mid-frequency band refers to the area between f_b and $f_{\rm sw}/2$, mainly including the resonant peak of the *LCL* filter. During the operation of the inverter, the current sampling signal is compared with the reference, the error passes through PI controller to form the modulation wave (voltage signal), and the low-frequency harmonic content in the modulation wave will change under the influence of closed-loop control. Next, in the pulsewidth modulation (PWM) process, the modulation wave is compared with the carrier wave to generate the pulse signal to control the ON–OFF of the power switch. Then, the inverter outputs the voltage pulse signal. It is obvious that the voltage pulse signal contains not only the above low-frequency harmonics, but also the sideband harmonics generated by PWM. Finally, the voltage pulse signal becomes the current signal through *LCL* filter. At the same time, the *LCL* filter filters out the high-frequency harmonics in the voltage pulse signal and introduces the resonant peak in the mid-frequency band. This process moves in circles until the system enters the steady state, and the harmonic content in the output current tends to be stable. The abovementioned process will be further described below under different switching frequencies in combination with Fig. 2.

When the switching frequency is high, the mid-frequency band is wide, and the working range of closed-loop control and filter is basically independent of each other. Harmonics affected by closed-loop control and harmonics generated by PWM will not enter the mid-frequency band. Therefore, even if the *LCL* filter will introduce resonant peak in the mid-frequency band, the resonant peak will not be coupled with the abovementioned harmonics, which is easy to be suppressed by AD. When the switching frequency is high, the harmonic characteristics in the inverter system are shown in Fig. 2(a).

When the switching frequency becomes low, the mid-frequency band becomes narrow, and the following two coupling

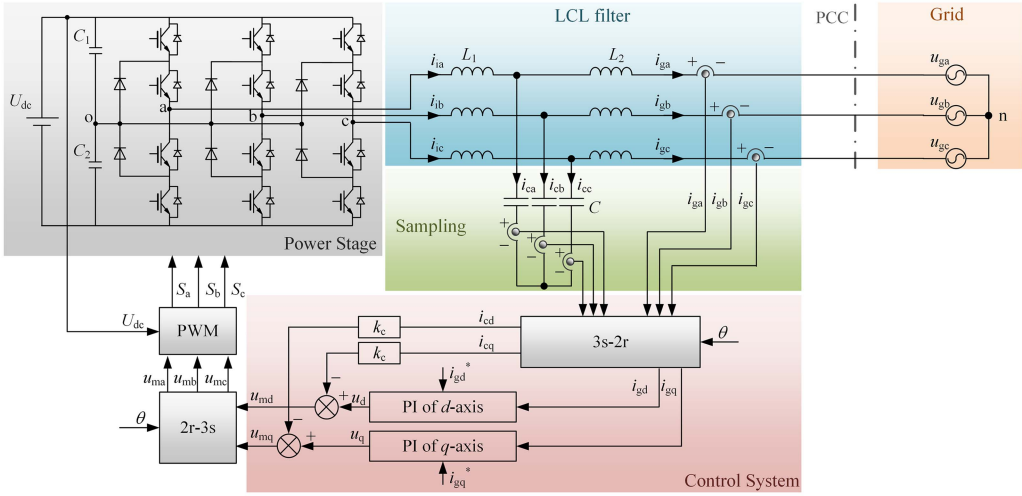

Fig. 1. *LCL* TL-NPC GCI system.

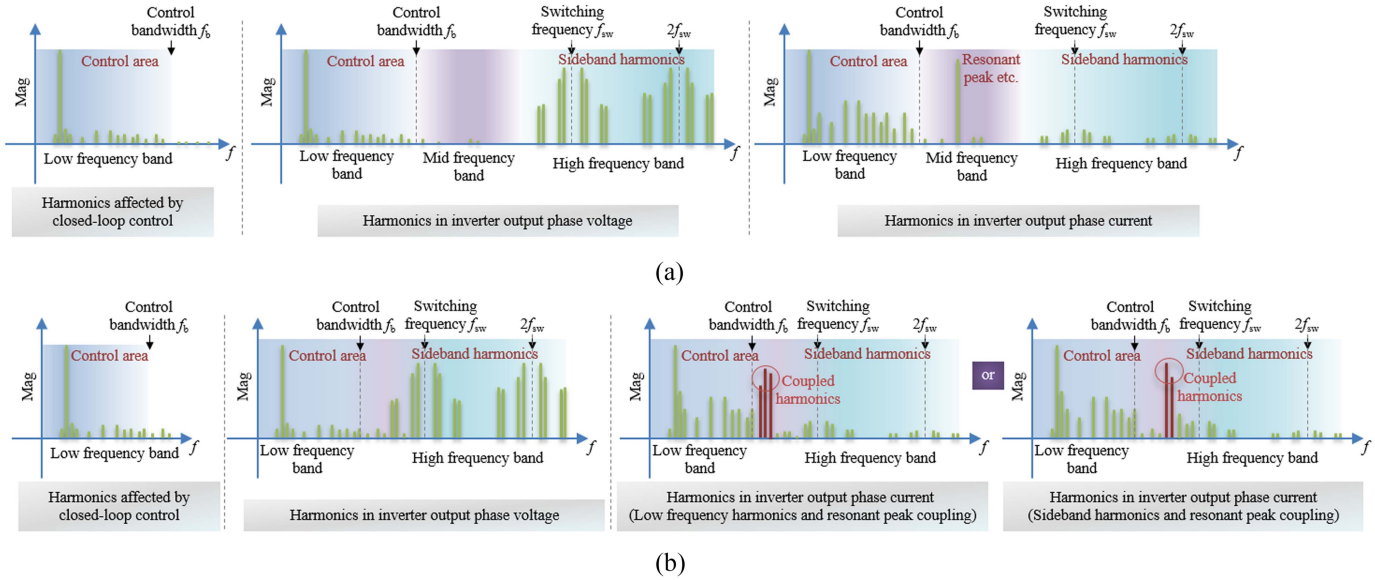

Fig. 2. Harmonic characteristics in GCI system. (a) Under high switching frequency. (b) Under low switching frequency.

modes may occur during the operation of inverter. First, when the resonant frequency of the *LCL* filter is relatively low, the resonant peak may be coupled with the low-frequency harmonics and amplify them. Second, when the resonant frequency of the *LCL* filter is relatively high, the resonant peak will be coupled with the sideband harmonics generated by PWM below the switching frequency and amplify them. Under LSF condition, the harmonic characteristics in the inverter system are shown in Fig. 2(b).

It can be seen, under LSF condition, the mid-frequency band narrows and the boundary of the three-frequency bands is no longer clear. The low-frequency harmonics under the impact of closed-loop control and the sideband harmonics lower than the switching frequency will enter mid-frequency area. Therefore, under the amplification effect of the resonant peak, the content and amplitude of harmonics in the mid-frequency band will increase, which is difficult to suppress even if AD is added. Therefore, the mid-frequency harmonic coupling under LSF is very complex, which will greatly affect the output waveform quality and system stability of the inverter. Obviously, the single-frequency model cannot reflect the coupling relationship between input and output harmonics. In addition, because the dominant frequencies of GCI is difficult to know, the GA modeling method is also difficult to complete the accurate modeling and harmonic characteristic analysis of LSF GCI. However, the core idea of HSS modeling is to express the input and output of the system in the form of each harmonic component, and convert periodic variables in the time domain into constants in the frequency domain through series decomposition, so as to construct the relationship between each input harmonic and each output harmonic. Thus, establishing HSS model is the best means to analyze the harmonic characteristics of LSF GCI.

C. Necessity to Consider the Impact of Digitization

Because the actual GCI system often adopts digital processor, digital controller is also adopted accordingly. However, digital control will inevitably introduce the control delay, which will change the phase characteristics of the system and affect the system stability. Especially under LSF condition, the problems brought by digitization have a more significant impact on system performance. This will be explained as follows. For the analog control system, sampling is carried out at time *k*, and the control signal and PWM pulse signal will also be updated at time *k*. obviously, the closed-loop control and PWM signal update in analog control are completed at the same time, so it has good control effect. However, in digital control, because the operation of codes such as coordinate transformation and algebraic calculation takes time, so the sampling is carried out at time *k*, and the control signal will be updated at time (*k*+1) (the time scale is the sampling period). We can find that since the control signal is not updated in time at time *k*, the PWM signal is not updated in time either. Hence, the PWM signal sent out at time *k* is calculated by the closed-loop control at time (*k*−1), it indicates that the digital control is "not timely." Especially in LSF GCI, the lower switching-frequency has already reduced the update frequency of PWM signal, then limited the settling speed and ability of inverter output, and greatly affected the inverter output performance. If there is still existing control delay at this time, the update of PWM signal will be more untimely, which will further affect the inverter output performance. In conclusion, the control delay cannot be ignored in the modeling work or model calculation and analysis of LSF GCI.

III. HSS Overview

HSS model belongs to harmonic-domain model [33], and is derived from the LTP model [34]. It converts periodic variables in time-domain model into constants in frequency domain through Fourier series, which greatly avoids the complex calculation in time domain. The modeling process of HSS is divided into the following six steps.

Step 1: use the linearization method to linearize the nonlinear model. Assuming that all time-varying signals in the system are periodic signals, construct the LTP model of the system, as shown in the following equation:

$$\begin{cases} \dot{x}(t) = A(t)x(t) + B(t)u(t) \\ y(t) = C(t)x(t) + D(t)u(t) \end{cases} \tag{1}$$

where *x(t)*, *u(t),* and *y(t)* are state variables, inputs, and outputs of the system, respectively. *A(t)*, *B(t)*, *C(t),* and *D(t)* are state matrix, input matrix, output matrix, and input–output matrix of the system, respectively.

Step 2: decompose state variables, inputs, and outputs in (1) into Fourier series. First, decompose the state variable

$$x(t) = e^{st} \sum_{n=-\infty}^{+\infty} x_n e^{jn\omega_1 t}. \tag{2}$$

In (2), the first part e^{st} ($s = \delta + j\omega$) is the exponentially modulated periodic (EMP) operator, and the second part is the Fourier series expression, where *xn* is the Fourier coefficient, ω_1 is the fundamental angular frequency. Because the Fourier series decomposition can only reflect the steady-state characteristics of the signal, in order to reflect the small transient characteristics of the signal, the EMP operator is introduced. And the differential form of the state variable is

$$\dot{x}(t) = \sum_{n=-\infty}^{+\infty} (jn\omega_1 + s)\, x_n e^{(jn\omega_1+s)t}. \tag{3}$$

Meanwhile, the input and output are also expressed in the form of (2), as follows:

$$u(t) = e^{st} \sum_{n=-\infty}^{+\infty} u_n e^{jn\omega_1 t}, \quad y(t) = e^{st} \sum_{n=-\infty}^{+\infty} y_n e^{jn\omega_1 t}. \tag{4}$$

Step 3: decompose *A(t)*, *B(t)*, *C(t),* and *D(t)* by Fourier series

$$\begin{aligned} A(t) &= \sum_{n=-\infty}^{+\infty} A_n e^{jn\omega_1 t}, \quad B(t) = \sum_{n=-\infty}^{+\infty} B_n e^{jn\omega_1 t} \\ C(t) &= \sum_{n=-\infty}^{+\infty} C_n e^{jn\omega_1 t}, \quad D(t) = \sum_{n=-\infty}^{+\infty} D_n e^{jn\omega_1 t}. \end{aligned} \tag{5}$$

Step 4: substitute (2)–(5) into (1), we can obtain

$$\begin{cases} \dot{X}(\omega,t) = A(\omega) \otimes X(\omega,t) + B(\omega) \otimes U(\omega,t) \\ \dot{Y}(\omega,t) = C(\omega) \otimes X(\omega,t) + D(\omega) \otimes U(\omega,t) \end{cases} \tag{6}$$

here, "⊗" represents convolution. Namely, we can use convolution in frequency domain to replace multiplication in time-domain model (1).

Step 5: simplify the convolution operation. Convolution operation is complex, in order to simplify it, convolution can be obtained from frequency matrix (e.g., Toeplitz matrix). In other words, the matrix containing periodic variables should be expressed in the form of Toeplitz matrix in the frequency-domain model, so that the convolution operation can be simplified. Assuming that *A(t)* in time-domain model (1) contains periodic variables, so matrix *A* should be expressed in the Toeplitz matrix form $\mathcal{A}$ in frequency-domain model. Thus, after simplifying the convolution operation, (6) can be expressed as

$$\begin{cases} \sum_{n=-\infty}^{+\infty} (jn\omega_1 + s)\, x_n e^{jn\omega_1 t + st} \\ \quad = \sum_{n,m=-\infty}^{+\infty} \mathcal{A}_{n-m} x_m e^{jn\omega_1 t + st} \\ \quad + \sum_{n,m=-\infty}^{+\infty} B_{n-m} u_m e^{jn\omega_1 t + st} \\ \sum_{n=-\infty}^{+\infty} y_n e^{jn\omega_1 t + st} = \sum_{n,m=-\infty}^{+\infty} C_{n-m} x_m e^{jn\omega_1 t + st} \\ \quad + \sum_{n,m=-\infty}^{+\infty} D_{n-m} u_m e^{jn\omega_1 t + st} \end{cases}. \tag{7}$$

Step 6*:* simplify (7) according to the harmonic balance principle, we can obtain

$$\begin{cases} (jm\omega_1 + s)\, X_n = \sum_{m=-\infty}^{+\infty} \mathcal{A}_{n-m} X_m + \sum_{m=-\infty}^{+\infty} B_{n-m} U_m \\ Y_n = \sum_{m=-\infty}^{+\infty} C_{n-m} X_m + \sum_{m=-\infty}^{+\infty} D_{n-m} U_m \end{cases} \tag{8}$$

namely

$$\begin{cases} sX_n = (\mathcal{A}_n - N)X_n + B_nU_n \\ Y_n = C_nX_n + D_nU_n \end{cases}. \tag{9}$$

Refer to [34] for the basic modeling theory of HSS. Where X_n, U_n, and Y_n are the forms of harmonic components of state variables, inputs, and outputs, respectively. For example, $Y_n = \ldots, Y_{-h}, Y_{-h+1}, \ldots, Y_{-1}, Y_0, Y_1, \ldots, Y_{h-1}, Y_h$. $\mathcal{A}$ is in the form of Toeplitz matrix, as follows:

$$\mathcal{A} = \begin{bmatrix} A_0 & A_{-1} & \cdots & A_{-h} & \\ A_1 & A_0 & A_{-1} & \ddots & A_{-h} \\ \vdots & A_1 & A_0 & A_{-1} & \vdots \\ A_h & \ddots & A_1 & A_0 & A_{-1} \\ & A_h & \cdots & A_1 & A_0 \end{bmatrix} \tag{10}$$

and N is the modulation frequency matrix

$$N = \text{diag}\left(\cdots\ -2j\omega_1\ -j\omega_1\ 0\ j\omega_1\ 2j\omega_1\ \cdots\right). \tag{11}$$

In addition, it should be noted that the outputs calculated by (9) are frequency-domain results. They can be transformed into time-domain results by the following equation:

$$y(t) = T(t)Y_n. \tag{12}$$

Where in

$$T(t) = \left[e^{-jh\omega_1 t}\ \cdots e^{-j2\omega_1 t}\ e^{-j\omega_1 t}\ 1\ e^{j\omega_1 t}\ e^{j2\omega_1 t} \cdots\ e^{jh\omega_1 t}\right]. \tag{13}$$

IV. Methods of Considering Digitization Impact Under Two Calculation and Analysis Methods of HSS Model

Facing the complex HSS model, it is very necessary to select the appropriate calculation and analysis method according to the research purpose. However, the current relevant literatures fail to conduct a thorough and detailed study on the modeling process, calculation and analysis methods of HSS according to different application backgrounds and research purposes. Based on this, this article studies two calculation and analysis methods of the HSS model, namely iterative calculation method and frequency-domain analysis method. The two calculation and analysis methods of the HSS model and their applications will be described as follows.

The iterative calculation method of the HSS model only needs to independently construct the HSS model of each part of GCI system, including the HSS model of closed-loop control, HSS model of main circuit (i.e., plant), etc. There is no need to integrate the HSS models of all parts into a whole, just assign corresponding initial values to each state variable and system input, and iteratively calculate the HSS model of each part in order. The iterative calculation method of HSS model can be used to replace the circuit simulation, to accurately calculate the harmonic components of inverter state variables, and can more intuitively reflect the system dynamic characteristics.

The frequency-domain analysis method of HSS model needs to integrate the HSS models of all parts of GCI system. In this way, the whole GCI system is finally expressed by a complete HSS model. Therefore, the HTF of the system can be easily obtained, and then the stability and rapidity of the system can be analyzed by frequency-domain analysis means, such as bode diagram, Nyquist diagram, and pole map.

As mentioned in Section I, the current relevant research fails to take into account the impact of digitization on the system. However, under LSF condition, the impact of digitization on system output is more significant and cannot be ignored (mentioned in Section II-C). Therefore, this section first describes the establishment process of the basic HSS model of the *LCL* GCI system. Then, under different calculation and analysis methods of the HSS model, two different methods considering the impact of digitization are proposed.

A. Basic HSS Model of LCL GCI

1) Main Circuit Model: First, starting with the single-phase *LCL* GCI, the nonlinear time-periodic model of the main circuit is

$$\begin{aligned} \begin{bmatrix} \dot{i}_i(t) \\ \dot{i}_g(t) \\ \dot{u}_c(t) \\ \dot{u}_{\text{dc}}(t) \end{bmatrix} &= \begin{bmatrix} 0 & 0 & -1/L_1 & 0 \\ 0 & 0 & 1/L_2 & 0 \\ 1/C & -1/C & 0 & 0 \\ s(t)/C_{\text{dc}} & 0 & 0 & -1/(R_{\text{dc}}C_{\text{dc}}) \end{bmatrix} \\ &\quad \times \begin{bmatrix} i_i(t) \\ i_g(t) \\ u_c(t) \\ u_{\text{dc}}(t) \end{bmatrix} \\ &\quad + \begin{bmatrix} u_{\text{dc}}(t)/(2L_1) & 0 & 0\ 0 \\ 0 & -1/L_2 & 0\ 0 \end{bmatrix}^{\text{T}} \begin{bmatrix} s(t) \\ u_g(t) \end{bmatrix} \\ i_g(t) &= \begin{bmatrix} 0\ 1\ 0\ 0 \end{bmatrix} \begin{bmatrix} i_i(t)\ i_g(t)\ u_c(t)\ u_{\text{dc}}(t) \end{bmatrix}^{\text{T}} \end{aligned} \tag{14}$$

here, superscript "T" represents the transpose matrix. According to linearization theory, we can obtain

$$\begin{cases} u_{\text{dc}}(t)s(t) = U_{\text{dc}} \triangle\ s(t) + S \triangle\ u_{\text{dc}}(t) \\ i_i(t)s(t) = I_i \triangle\ s(t) + S \triangle\ i_i(t) \end{cases} \tag{15}$$

where "$\triangle$" represents the deviation. Therefore, the linearized model of the main circuit is

$$\begin{aligned} \begin{bmatrix} \triangle \dot{i}_i(t) \\ \triangle \dot{i}_g(t) \\ \triangle \dot{u}_c(t) \\ \triangle \dot{u}_{\text{dc}}(t) \end{bmatrix} &= \begin{bmatrix} 0 & 0 & -1/L_1 & S/(2L_1) \\ 0 & 0 & 1/L_2 & 0 \\ 1/C & -1/C & 0 & 0 \\ S/C_{\text{dc}} & 0 & 0 & -1/(R_{\text{dc}}C_{\text{dc}}) \end{bmatrix} \\ &\quad \times \begin{bmatrix} \triangle i_i(t) \\ \triangle i_g(t) \\ \triangle u_c(t) \\ \triangle u_{\text{dc}}(t) \end{bmatrix} \\ &\quad + \begin{bmatrix} U_{\text{dc}}/2L_1 & 0 & 0\ I_i/C_{\text{dc}} \\ 0 & -1/L_2 & 0\ 0 \end{bmatrix}^{\text{T}} \begin{bmatrix} \triangle s(t) \\ \triangle u_g(t) \end{bmatrix} \\ \triangle i_g(t) &= \begin{bmatrix} 0\ 1\ 0\ 0 \end{bmatrix} \begin{bmatrix} \triangle i_i(t)\ \triangle i_g(t)\ \triangle u_c(t)\ \triangle u_{\text{dc}}(t) \end{bmatrix}^{\text{T}}. \end{aligned} \tag{16}$$

Next, the linearized model of single-phase *LCL* GCI is extended to three-phase system. The state variables, inputs, and

outputs of the main circuit of three-phase *LCL* GCI is

$$\Delta x_{im} = \left[\triangle i_{ia}(t) \triangle i_{ib}(t) \triangle i_{ic}(t) \triangle i_{ga}(t) \triangle i_{gb}(t) \triangle i_{gc}(t) \triangle u_{ca}(t) \triangle u_{cb}(t) \triangle u_{cc}(t) \triangle u_{\mathrm{dc}}(t)\right]^{\mathrm{T}}$$

$$\Delta u_{im} = \begin{bmatrix} \triangle s_a(t) & \triangle s_b(t) & \triangle s_c(t) \\ \triangle u_{ga}(t) & \triangle u_{gb}(t) & \triangle u_{gc}(t) \end{bmatrix}^{\mathrm{T}}$$

$$\Delta y_{im} = \left[\triangle i_{ga}(t) \triangle i_{gb}(t) \triangle i_{gc}(t)\right]^{\mathrm{T}}.$$

Then, the linearized model of the main circuit of three-phase *LCL* GCI is

$$\begin{cases} \Delta \dot{x}_{im}(t) = A_i(t)\Delta x_{im}(t) + B_i(t)\Delta u_{im}(t) \\ \Delta y_{im}(t) = C_i(t)\Delta x_{im}(t) \end{cases} \tag{17}$$

where the expressions of matrices $A_{\mathrm{i}}(t)$, $B_{\mathrm{i}}(t)$, and $C_{\mathrm{i}}(t)$ are shown in (A1) of the Appendix.

2) Control System Model: The *LCL* GCI studied in this article adopts GCF PI + CCF AD. Suppose

$$\begin{cases} \Delta \dot{e}_d(t) = \Delta i^*_{gd}(t) - \Delta i_{gd}(t) \\ \Delta \dot{e}_q(t) = \Delta i^*_{gq}(t) - \Delta i_{gq}(t) \end{cases} \tag{18}$$

where the superscript "*" represents the reference. Let the state variables, inputs, and outputs of the control system are

$$\Delta x_{ic}(t) = \left[\Delta e_d(t)\ \Delta e_q(t)\right]^{\mathrm{T}}$$

$$\Delta u_{ic}(t) = \left[\Delta i^*_{ga}(t)\ \Delta i^*_{gb}(t)\ \Delta i^*_{gc}(t)\ \Delta i_{ia}(t)\ \Delta i_{ib}(t)\ \Delta i_{ic}(t)\ \Delta i_{ga}(t)\ \Delta i_{gb}(t)\ \Delta i_{gc}(t)\right]^{\mathrm{T}}$$

$$\Delta y_{ic}(t) = \left[\Delta s_a(t)\ \Delta s_b(t)\ \Delta s_c(t)\right]^{\mathrm{T}}.$$

Then, the state-space equation of the control system is

$$\begin{cases} \Delta \dot{x}_{ic}(t) = E_i(t)\Delta x_{ic}(t) + F_i(t)\Delta u_{ic}(t) \\ \Delta y_{ic}(t) = G_i(t)\Delta x_{ic}(t) + H_i(t)\Delta u_{ic}(t) \end{cases} \tag{19}$$

where the expressions of $E_{\mathrm{i}}(t)$, $F_{\mathrm{i}}(t)$, $G_{\mathrm{i}}(t)$, and $H_{\mathrm{i}}(t)$ are shown in (A2) of the Appendix.

3) Basic HSS Model of LCL GCI: According to the modeling process of HSS in Section III, combined with (17) and (19), HSS models of the main circuit and control system are

$$\begin{cases} \dot{X}_{imh} = (\mathcal{A}_{ih} - N_m)X_{imh} + \mathcal{B}_{ih}U_{imh} \\ Y_{imh} = C_{ih}X_{imh} \end{cases} \tag{20}$$

$$\begin{cases} \dot{X}_{ich} = (E_{ih} - N_c)X_{ich} + \mathcal{F}_{ih}U_{ich} \\ Y_{ich} = \mathcal{G}_{ih}X_{ich} + \mathcal{H}_{ih}U_{ich} \end{cases}. \tag{21}$$

The state variables, inputs, and outputs in (20) and (21) are in the form of harmonic components of state variables, inputs, and outputs in (17) and (19). Assuming that the truncation number is r, so the form of the state variable matrix X_{imh} is

$$X_{imh} = \left[\triangle i_{ia\_-r\sim r} \triangle i_{ib\_-r\sim r} \triangle i_{ic\_-r\sim r} \triangle i_{ga\_-r\sim r} \triangle i_{gb\_-r\sim r} \triangle i_{gc\_-r\sim r} \triangle u_{ca\_-r\sim r} \triangle u_{cb\_!-r\sim r} \triangle u_{cc\_-r\sim r} \triangle u_{dc\_-r\sim r}\right]^{\mathrm{T}}$$

where

$$\Delta i_{ia\_-r\sim r} = \left[\Delta i_{ia\_-r}\ \Delta i_{ia\_-(r-1)} \cdots \Delta i_{ia\_0} \right]^{\mathrm{T}}$$

The forms of other state variables, inputs, and outputs are similar, and the dimensions of frequency modulation matrices N_m and N_c are the same as matrices $\mathcal{A}_{ih}$ and E_{ih}, respectively. Since the elements in the matrices C_{ih} and E_{ih} are constants, the form of C_{ih} is shown in (22), and the form of E_{ih} is similar

$$C_{ih} = \mathrm{diag}\left(C_{i\_-r} \cdots C_{i\_-1}\ C_{i0}\ C_{i\_1} \cdots C_{i\_r}\right). \tag{22}$$

However, since $\mathcal{A}_{ih}, \mathcal{B}_{ih}, \mathcal{F}_{ih}, \mathcal{G}_{ih}$, and $\mathcal{H}_{ih}$ contain periodic variables such as switching function, inverter-side current, and Park transformation, the abovementioned matrix needs to be expressed in the form of Toeplitz matrix, as shown in (10).

B. Method Considering the Impact of Digitization Under Iterative Calculation Method

The traditional iterative calculation process of the HSS model is as follows. First, set the initial values of the state variables of control system (21), set the reference. Meanwhile, in the plant (20), set the initial values of the state variables and the switching function S_x, set the grid voltage. Here, the initial value of S_x is calculated by double Fourier series, so the modulation strategy will affect the distribution and content of the initial value of sideband harmonics lower than the switching frequency. At LSF, the abovementioned sideband harmonics will be coupled with other harmonics in the mid-frequency region. Therefore, the current harmonic content in the mid-frequency region will be affected by the modulation strategy. Then, calculate the complete response of (21) and update the state variables. Finally, take the output signal of the control system and the grid voltage signal as the inputs of the plant (20), calculate the complete response of (20) and update its state variables. At the same time, update the feedback signal required by (21). Repeat the abovementioned process to complete the iteration. It is obvious that the abovementioned traditional iterative-process does not take into account the impact of switching frequency, S/H, and control delay on system characteristics. Therefore, there is some deviation between the results obtained from the traditional iterative-calculation-process of HSS model and the circuit simulation, which cannot completely replace the circuit simulation results. Based on this problem, the iterative process of HSS model is improved in this article. The iterative calculation process of the HSS model considering the digitization impact and switching frequency proposed in this article is shown in Fig. 3. The following is the specific description of Fig. 3.

First, the sampling period T_{s} of the system is reflected by setting the time length of the complete response process of solving the differential equation, that is, to solve the complete response of the differential equation within T_s. This improvement is reflected by steps $s2$ and $s5$ in Fig. 3.

Second, the switching frequency of the system is reflected by setting the update frequency of the input signal U_{imh} of plant (20). Here, U_{imh} includes switching function s_x. This improvement is reflected by steps $s3$, $s4$, and $s8$ in Fig. 3. The part in the dotted box in Fig. 3 is completed in one sampling period, that is, the sampling period is the unit time length in the iterative process. Meanwhile, the switching frequency is the update frequency of the PWM signal, that is, the update frequency of the switching function. It can be seen, the switching function can be updated

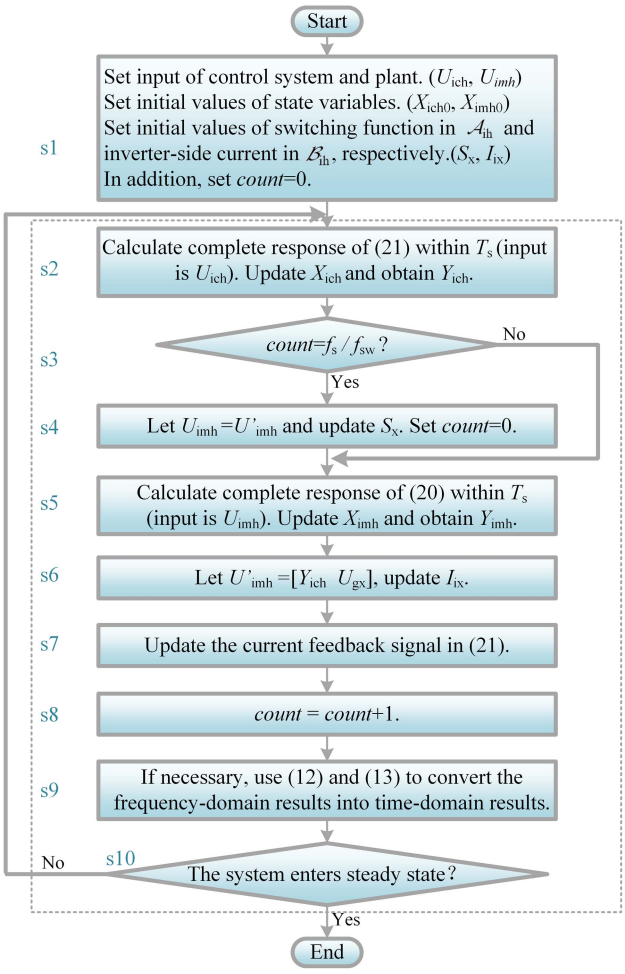

Fig. 3. Iterative calculation process of HSS model considering digitization impact and switching frequency.

the update frequency of the switching function is f_{sw}. In this way, the switching frequency is reflected in the iterative process.

Finally, use the Y_{ich} calculated in the previous sampling period to update the input U_{imh} of $s5$, so as to reflect the one-beat control delay. This improvement is reflected by steps $s5$ and $s6$ in Fig. 3. According to the closed-loop control process of GCI, theoretically, the output signal calculated in step $s2$ is the input of the differential (20) in step $s5$. However, in the design idea of Fig. 3, the output signal Y_{ich} (including the switching function s_x) of step $s2$ is not immediately assigned to the input signal U_{imh} of $s5$. Instead, execute $s5$ first, and then update the input U_{imh} of $s5$. It can be found, when the input U_{imh} of $s5$ needs to be updated, the Y_{ich} calculated in the previous sampling period is used to update U_{imh}, so the simulation of one-beat control delay is realized.

In the following, an example will be given to illustrate the improved iterative-process considering the digitization impact and switching frequency. Suppose $f_{sw} = 2$ kHz, $f_s = 6$ kHz.

Within first T_s: Execute $s1$, $s2$, $s5$, $s6$, $s7$, $s8$, $s9$, and $s10$. The input of $s5$ is U_{imh0}. After execution, $U'_{imh} = U_{imh1}$, *count* $= 1$.

Within second T_s: Execute $s2$, $s5$, $s6$, $s7$, $s8$, $s9$, and $s10$. The input of $s5$ is U_{imh0}. After execution, $U'_{imh} = U_{imh2}$, *count* $= 2$.

Within third T_s: Execute $s2$, $s5$, $s6$, $s7$, $s8$, $s9$, and $s10$. The input of $s5$ is U_{imh0}. After execution, $U'_{imh} = U_{imh3}$, *count* $= 3$.

Within fourth T_s: Execute $s2$–$s10$. The input of $s5$ is U_{imh3}. After execution, $U'_{imh} = U_{imh4}$, *count* $= 1$.

Within fifth T_s: Execute $s2$, $s5$, $s6$, $s7$, $s8$, $s9$, and $s10$. The input of $s5$ is U_{imh3}. After execution, $U'_{imh} = U_{imh5}$, *count* $= 2$.

Within sixth T_s: execute $s2$, $s5$, $s6$, $s7$, $s8$, $s9$, and $s10$. The input of $s5$ is U_{imh3}. After execution, $U'_{imh} = U_{imh6}$, *count* $= 3$.

Within seventh T_s: execute $s2$–$s10$. The input of $s5$ is U_{imh6}. After execution, $U'_{imh} = U_{imh7}$, *count* $= 1$.

……

In the abovementioned example, U_{imh} (including switching function s_x) is updated every three T_s, that is, the switching function s_x is updated every T_{sw}, reflecting the consideration of switching frequency. Meanwhile, every time the input U_{imh} of $s5$ is updated, Y_{ich} calculated in the previous sampling period is used to update U_{imh}, which reflects the control delay of one beat.

C. Method Considering the Impact of Digitization Under Frequency-Domain Analysis Method

A complete closed-loop HSS model of GCI needs to be constructed under the frequency-domain analysis method. Therefore, it is necessary to use the corresponding state-space model to represent S/H and control delay, and need to merge the state-space equations of nonideal unit, main circuit, and closed-loop control system. The construction process of the complete HSS model of GCI considering the digitization impact will be described as follows. Since the linearized models of main circuit and control system have been described in Section IV-A, the state-space model of non-ideal unit and the complete HSS model of the whole system will be mainly described as follows.

In digital control system of GCI, the sampling switch and holder exist at the same time, the expression of S/H is

$$G_{s\&h}(s) = e^{-0.5sT_s}. \tag{23}$$

The mathematical expression of one-beat control delay is

$$G_c(s) = e^{-sT_s}. \tag{24}$$

The first-order Pade approximation is used to approximate the delay in (23) and (24). The expression of the first-order Pade approximation is

$$e^{-a_d s} \approx \frac{1 - a_d s}{1 + a_d s}. \tag{25}$$

Thus, it can be obtained from (23) to (25)

$$\begin{cases} a_d = 0.25T_s, & \text{consider S/H only} \\ a_d = 0.5T_s, & \text{consider control delay only} \\ a_d = 0.75T_s, & \text{consider S/H and control delay} \end{cases}. \tag{26}$$

It can be seen that whether only S/H or control delay or all the abovementioned units are considered, they can be represented by a general model. Here, let the state variables, inputs, and

outputs of nonideal unit be

$$\Delta x_{id}(t) = \left[\Delta x_{idd}(t)\ \Delta x_{idq}(t)\right]^{\mathrm{T}}$$
$$\Delta u_{id}(t) = \left[\Delta s_{1d}(t)\ \Delta s_{1q}(t)\right]^{\mathrm{T}}$$
$$\Delta y_{id}(t) = \left[\triangle\ s_a(t)\ \triangle\ s_b(t)\ \triangle\ s_c(t)\right]^{\mathrm{T}}.$$

So the model of nonideal unit is

$$\begin{cases} \Delta\dot{x}_{id}(t) = I_i(t)\Delta x_{id}(t) + J_i(t)\Delta u_{id}(t) \\ \Delta y_{id}(t) = K_i(t)\Delta x_{id}(t) + L_i(t)\Delta u_{id}(t) \end{cases} \tag{27}$$

where the expressions of $I_i(t)$, $J_i(t)$, $K_i(t)$, and $L_i(t)$ are shown in (A3) of the Appendix.

In order to facilitate the construction of the complete HSS model of the system, the state-space model of control system, nonideal unit, and main circuit will be reconstructed as follows.

First, the control system model is reconstructed according to (19) as follows:

$$\begin{cases} \Delta\dot{x}_c(t) = E_s(t)\begin{bmatrix}\triangle\ x_{im}(t)\\ \triangle\ x_{ic}(t)\\ \triangle\ x_{id}(t)\end{bmatrix} + F_s(t)\Delta u_c(t) \\ \Delta y_c(t) = G_s(t)\begin{bmatrix}\triangle\ x_{im}(t)\\ \triangle\ x_{ic}(t)\\ \triangle\ x_{id}(t)\end{bmatrix} + H_s(t)\Delta u_c(t) \end{cases} \tag{28}$$

where

$$\Delta x_c(t) = \Delta x_{ic}(t),$$
$$\Delta u_c(t) = \left[\Delta i^*_{ga}(t)\ \Delta i^*_{gb}(t)\ \Delta i^*_{gc}(t)\ \Delta u_{ga}(t)\ \Delta u_{gb}(t)\ \Delta u_{gc}(t)\right]^{\mathrm{T}}$$
$$\Delta y_c(t) = \left[\Delta s_{1d}(t)\ \Delta s_{1q}(t)\ \Delta u_{gd}(t)\ \Delta u_{gq}(t)\right]^{\mathrm{T}}.$$

Second, according to (27), the model of the non-ideal unit is reconstructed as follows:

$$\begin{cases} \Delta\dot{x}_d(t) = I_s(t)\begin{bmatrix}\triangle\ x_{im}(t)\\ \triangle\ x_{ic}(t)\\ \triangle\ x_{id}(t)\end{bmatrix} + J_s(t)\Delta u_d(t) \\ \Delta y_d(t) = K_s(t)\begin{bmatrix}\triangle\ x_{im}(t)\\ \triangle\ x_{ic}(t)\\ \triangle\ x_{id}(t)\end{bmatrix} + L_s(t)\Delta u_d(t) \end{cases} \tag{29}$$

where

$$\Delta x_d(t) = \Delta x_{id}(t),\ \Delta u_d(t) = \Delta y_c(t)$$
$$\Delta y_d(t) = \left[\Delta s_a(t)\ \Delta s_b(t)\ \Delta s_c(t)\ \Delta u_{ga}(t)\ \Delta u_{gb}(t)\ \Delta u_{gc}(t)\right]^{\mathrm{T}}.$$

Finally, according to (17), the main circuit model is reconstructed as follows:

$$\begin{cases} \Delta\dot{x}_m(t) = A_s(t)\begin{bmatrix}\triangle\ x_{im}(t)\\ \triangle\ x_{ic}(t)\\ \triangle\ x_{id}(t)\end{bmatrix} + B_s(t)\Delta u_m(t) \\ \Delta y_m(t) = C_s(t)\begin{bmatrix}\triangle\ x_{im}(t)\\ \triangle\ x_{ic}(t)\\ \triangle\ x_{id}(t)\end{bmatrix} \end{cases} \tag{30}$$

where

$$\Delta x_m(t) = \Delta x_{im}(t), \Delta u_m(t) = \Delta y_d(t)$$
$$\Delta y_m(t) = \Delta y_{im}(t).$$

Combining (28)–(30), the linearized model of *LCL* GCI based on GCF PI + CCF AD and considering the digitization impact can be obtained

$$\begin{cases} \Delta\dot{x}_p(t) = A_p(t)\Delta x_p(t) + B_p(t)\Delta u_p(t) \\ \Delta y_p(t) = C_p(t)\Delta x_p(t) \end{cases} \tag{31}$$

where

$$\Delta x_p(t) = \begin{bmatrix}\Delta x_m(t)\\ \Delta x_c(t)\\ \Delta x_d(t)\end{bmatrix},\ \Delta u_p(t) = \Delta u_c(t),\ \Delta y_p(t) = \Delta y_m(t)$$

$$A_p = \begin{bmatrix} A_s(t) + B_s(t)[K_s(t) + L_s(t)G_s(t)] \\ I_s(t) + J_s(t)G_s(t) \\ E_s(t) \end{bmatrix}$$

$$B_p = \begin{bmatrix} B_s(t)L_s(t)H_s(t) \\ J_s(t)H_s(t) \\ F_s(t) \end{bmatrix},\quad C_p = \left[C_s(t)\ Z_{1\times 2}\ Z_{1\times 2}\right].$$

The expressions of $A_s(t)$, $B_s(t)$, $C_s(t)$, $E_s(t)$, $F_s(t)$, $G_s(t)$, $H_s(t)$, $I_s(t)$, $J_s(t)$, $K_s(t)$, and $L_s(t)$ are shown in (A4), (A5), and (A6) of Appendix A.

Finally, according to HSS modeling process in Section III, the complete HSS model of *LCL* GCI based on GCF PI + CCF AD and considering digitization impact can be obtained from (31), namely

$$\begin{cases} \dot{X}_h = (\mathcal{A}_h - N_h)X_h + \mathcal{B}_h U_h \\ Y_h = C_h X_h \end{cases} \tag{32}$$

where the expression forms of each matrix and variables can refer to Section IV-A, which will not be repeated here. The closed-loop HTF of GCI can be obtained from (32), namely

$$G_{\mathrm{HTF}} = C_h[sI - (\mathcal{A}_h - N_h)]^{-1}\mathcal{B}_h. \tag{33}$$

V. Characteristic Analysis and Simulation Verification

This article will focus on the analysis and verification of the harmonic gain diagrams and pole maps of i_{gx}/i^*_{gx} and i_{gx}/u_{gx}. This article does not involve the research on the dc side because of the limited length, thus, it is assumed that the dc side is an ideal voltage source. If it is necessary to analyse the characteristics between dc side and ac side, it can be achieved by applying disturbance to dc-side voltage. In this section, the system characteristic analysis and simulation verification will be completed under two groups of system parameters. The system parameters are shown in Tables I and II. Among them, Table I shows the system parameters commonly used by the centralized photovoltaic GCI. However, due to the large power of the inverter, it is difficult to meet the laboratory conditions, so Table II is added to complete the corresponding experimental verification. This section will complete the following works under two groups of system parameters. First, the accuracy of

TABLE I
SYSTEM PARAMETER I

Parameter	Value
Power (P)	100 kW
DC-side voltage (U_{dc})	700 V
Grid voltage ($u_{g\_lineRMS}$)	315 V
Switching frequency (f_{sw})	2 kHz / 5 kHz
Sampling frequency (f_s)	8 kHz / 10 kHz
Filter parameters (L_1, L_2, C)	0.6 mH, 0.3 mH,100 μF / 0.4 mH, 0.2 mH,100 μF
Control parameters (k_p, k_i, k_c)	1.5, 2500,1.2 / 1.5, 2500, 2

TABLE II
SYSTEM PARAMETER II

Parameter	Value
Power (P)	1.2 kW
DC-side voltage (U_{dc})	130 V
Grid voltage ($u_{g\_lineRMS}$)	52 V
Switching frequency (f_{sw})	2 kHz / 5 kHz
Sampling frequency (f_s)	8 kHz / 10 kHz
Filter parameters(L_1, L_2, C)	3.5 mH, 1.75 mH, 15 μF / 2.5 mH, 1.25 mH, 15 μF
Control parameters (k_p, k_i, k_c)	1.5, 2500, 6 / 1.5, 2500, 8

the proposed iterative-calculation-method of HSS model considering digitization impact and switching frequency is verified. Second, based on the proposed inverter complete-HSS-model considering the digitization impact, the harmonic characteristics and stability of GCI are analyzed by frequency-domain analysis methods, and the necessity of considering the impact of digitization is explained.

As described in Section II, in the LSF system, the harmonic coupling occurs in the mid-frequency region, however, there are only sideband harmonics generated by modulation in the region higher than the switching frequency. Therefore, the harmonic characteristics within the switching frequency are more complex, which should be analyzed in detail. In the following content, this article focuses on the GCI with switching frequency of 2 kHz, so the truncation number of HSS model is set to 40. Here, one point needs to be explained. In Section V-A, the numerical simulation of 5 kHz GCI is introduced as a comparison. When f_{sw} is 5 kHz, the inverter output harmonics are mainly low-frequency harmonics, thus, the inverter HSS model with the truncation number of 40 can also basically reflect the harmonic characteristics of 5 kHz GCI.

A. Accuracy Verification of Iterative Calculation Method of HSS Model Considering Digitization Impact and Switching Frequency

Under different system parameters and switching frequencies, the dynamic waveforms of grid-side current obtained by different ways are shown in Figs. 4 and 5. Among them, the solid line represents the waveform obtained by Simulink circuit simulation under digital control (including S/H and control delay); the dotted line represents the waveform obtained by SSAV model and traditional iterative-method; the dash line represents the waveform obtained by HSS model and traditional iterative-method; the dash dot line represents the waveform obtained by HSS model and the iterative-method considering digitization impact and switching frequency.

First, combining Figs. 4 and 5, the dynamic waveform calculated by SSAV model has large error compared with other waveforms. It can only reflect the characteristics of fundamental component (i.e., the dc component in the rotating coordinate system) of grid-side current and cannot reflect the characteristics of other harmonic components. Thus, the limitation of the single-frequency model is verified. That is, it can only calculate the amplitude of the output signal with the same frequency as the reference signal, it is difficult to calculate the content of other output harmonics.

Next, in Figs. 4(a) and 5(a), the dynamic waveforms obtained by HSS model and different iterative-calculation-methods are compared. It can be seen that in the case of high switching frequency, the impact of digitization on the system is not very significant. Therefore, under high switching frequency, the harmonic components of grid-side current calculated by the traditional iterative-method based on the HSS model is also accurate.

Finally, in Figs. 4(b) and 5(b), the dynamic waveforms obtained by HSS model and different iterative-calculation-methods are compared. It is obvious that when the switching frequency is low, the dynamic waveform calculated by HSS model and the proposed iterative-method is more consistent with the Simulink circuit simulation waveform. It shows that when the switching frequency is low, the impact of digitization on system harmonic characteristics is great and cannot be ignored.

In conclusion, compared with the SSAV model, the HSS model can calculate each harmonic component of state variables. Under LSF condition, digitization has a great impact on the output harmonic characteristics of the system. Therefore, in the process of calculation and analysis of the HSS model, it is necessary to consider the influence of digitization and switching frequency on system characteristics. At the same time, through the abovementioned comparative analysis, it can be seen, no matter in the dynamic process or in the steady-state process, the HSS iterative-calculation-method considering the digitization impact and switching frequency proposed in this article is very accurate.

B. Frequency-Domain Analysis Based on Complete HSS Model of GCI

In the following characteristic analysis and simulation analysis, the switching frequency of *LCL* GCI is 2 kHz.

1) Frequency-Domain Analysis Under System Parameter I:

a) Characteristic Analysis Based on Harmonic Gain Diagram: The harmonic gain diagram is obtained from bode diagrams between the input and output components of all frequencies of the system. First, bode diagrams of HTF of the closed-loop system are drawn according to (33), and then the low-frequency gains of all bode diagrams are extracted to obtain the harmonic gain diagrams. Based on the complete HSS model of GCI including S/H and control delay established in this article, the harmonic gain diagrams of i_{ga}/i_{ga}^* and i_{ga}/u_{ga} are shown in Fig. 6. Among them, Fig. 6(a) and (b) is the harmonic gain diagrams between the input and output of the same frequency of

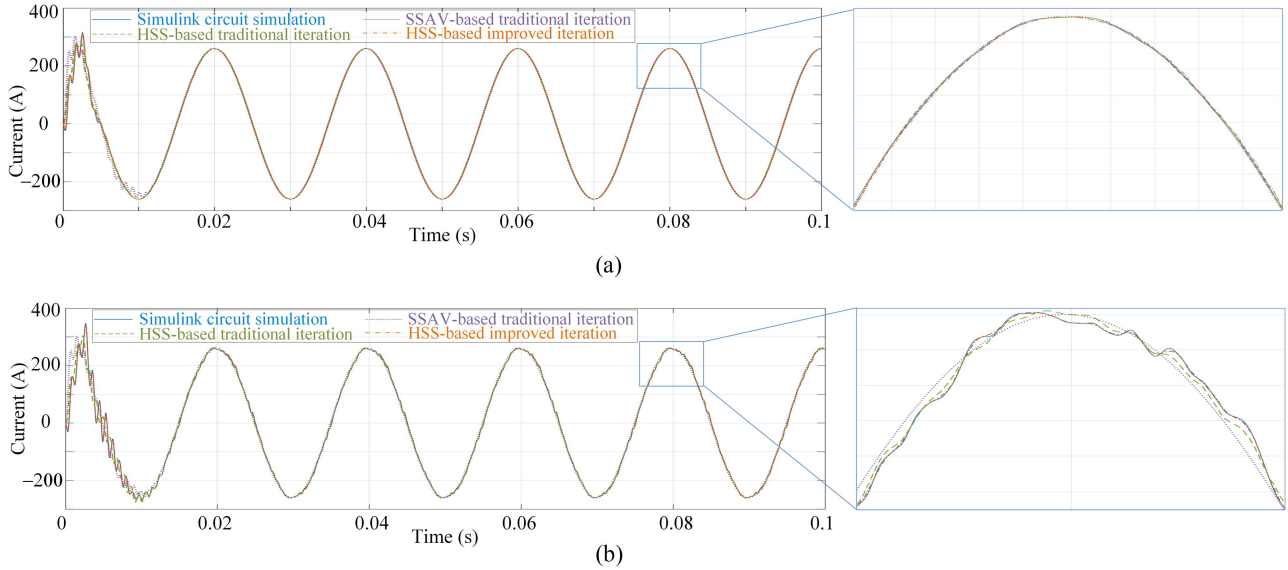

Fig. 4. Dynamic waveforms of grid-side current obtained by different methods under system parameter I. (a) $f_{\mathrm{sw}} = 5$ kHz. (b) $f_{\mathrm{sw}} = 2$ kHz.

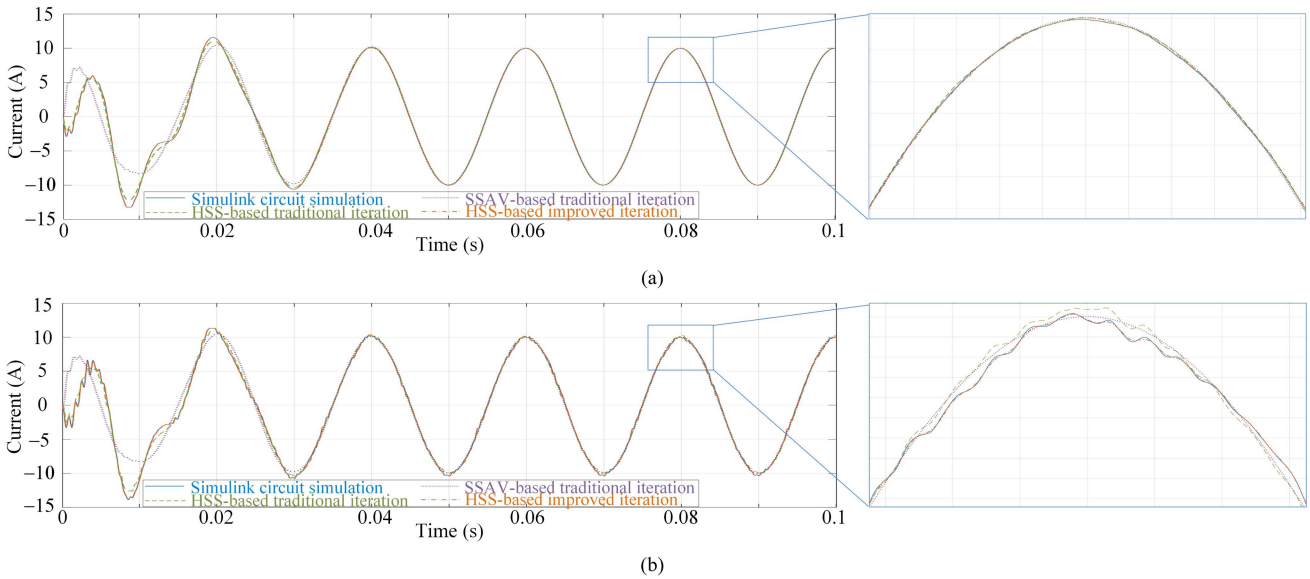

Fig. 5. Dynamic waveforms of grid-side current obtained by different methods under system parameter II. (a) $f_{\mathrm{sw}} = 5$ kHz. (b) $f_{\mathrm{sw}} = 2$ kHz.

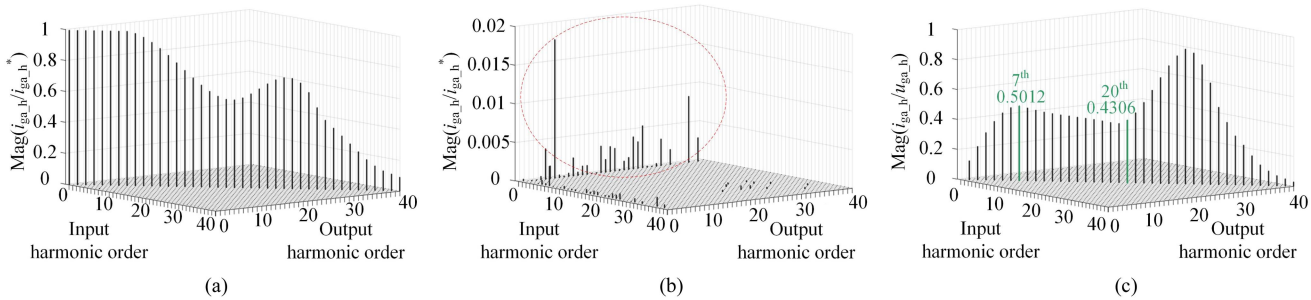

Fig. 6. Harmonic gain diagrams of GCI considering the impact of digitization. (a) Uncoupled term of i_{ga}/i_{ga}^{*}. (b) Coupled term of i_{ga}/i_{ga}^{*}. (c) i_{ga}/u_{ga}.

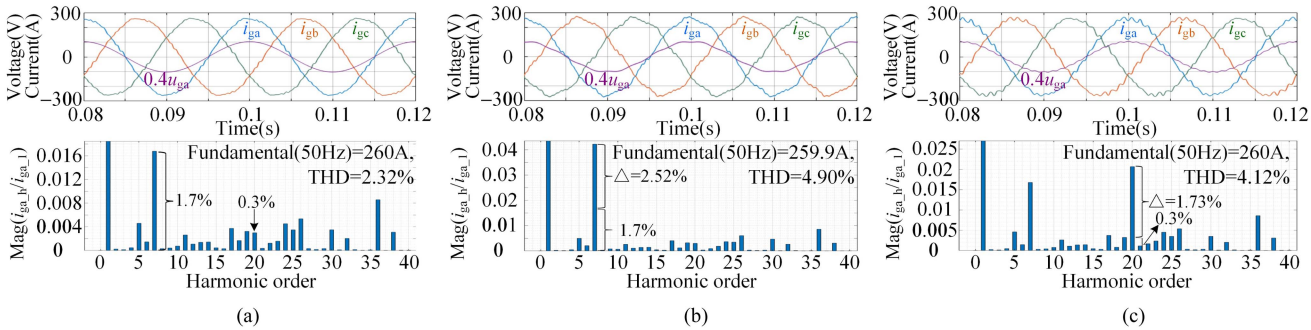

Fig. 7. Simulink circuit simulation waveforms and spectrums. (a) Under ideal grid. (b) Inject 5% seventh harmonic into grid. (c) Inject 4% 20th harmonic into grid.

i_{ga}/i^*_{ga}, and the harmonic gain diagram between the input and output of different frequencies of i_{ga}/i^*_{ga}, respectively. As can be seen from Fig. 6(a), the gain between the input and output of the same frequency attenuates to 0.7 at the 14th harmonic, indicating that the system control bandwidth is approximately 700 Hz. It is obvious that the information reflected in Fig. 6(a) is the information reflected by the inverter closed-loop bode diagram based on the SSAV model. As for Fig. 6(b), it contains non-diagonal information, namely coupling information. It shows that the established model can clearly reflect the relationship between the reference and the output harmonic components. Fig. 6(c) shows the harmonic gain diagram of i_{ga}/u_{ga}. It can be seen from the figure, there is no harmonic coupling between the grid-side current and the grid voltage in the same phase. Namely, the harmonics in the grid will only affect the output current component with the same frequency. The accuracy of Fig. 6 will be verified by Simulink circuit simulation results as follows.

Fig. 7 shows the Simulink simulation waveforms and spectrums of grid-side current. Here, the circuit simulation is based on digital control, including S/H and control delay modules. In the ideal grid, it can be seen from Fig. 7(a), the spectrum obtained by circuit simulation is basically consistent with the analytical results in the red box of Fig. 6(b). This shows that the complete HSS model considering digitization impact proposed in this article is accurate. Based on Figs. 6(b) and 7(a), the necessity of HSS modeling for LSF GCI will be explained by the way. When the switching frequency is 2 kHz, the sideband harmonics generated by modulation and lower than the switching frequency are 18th, 20th, 24th, 26th, 30th, 32nd, 36th, and 38th harmonics. If there is no harmonic coupling, the sideband harmonics can be obtained by double Fourier series. Thus, according to (7) and (9) in [35], the ratio of the abovementioned sideband harmonics to the fundamental wave is as follows: 0.0015, 0.0027, 0.0055, 0.0027, 0.0021, 0.0024, 0.0074, and 0.0034. But from Figs. 7(a) and 6(b), the ratio of the abovementioned sideband harmonics to the fundamental wave is actually: 0.0017, 0.0030, 0.0045, 0.0054, 0.0035, 0.0020, 0.0086, and 0.0031. Obviously, there are great differences between the two groups of data corresponding to 20th, 26th, 30th, and 36th harmonics. This is caused by harmonic coupling. It illustrates that under LSF, the sideband harmonics below the switching frequency enters the mid frequency region and is coupled with the resonant peak, even with the control loop, which affects the amplitude of these harmonics. It can be seen, it is difficult to reflect the actual amplitude of these sideband harmonics by double Fourier series under this condition. Therefore, HSS model should be used to analyze the output harmonic characteristics of inverter under LSF, which proves the correctness of the theoretical analysis in Section II-B.

Fig. 7(b) shows the inverter output waveforms and spectrum after injecting 5% seventh harmonic into the grid ($u_{g\_7\_\mathrm{peak}} = 12.85$ V). After injecting the harmonic, the seventh harmonic in the grid-side current increases by 2.52%, so $\triangle i_{\mathrm{ga}\_7}/\triangle u_{\mathrm{ga}\_7}$ is 0.5099, which is basically consistent with the result in Fig. 6(c). Finally, injecting 4% 20th harmonic ($u_{g\_20\_\mathrm{peak}} = 10.28$ V) into the grid, and the inverter output waveform and spectrum are shown in Fig. 7(c). It can be seen, the 20th harmonic of the grid-side current increases by 1.73%, so $\triangle i_{\mathrm{ga}\_20}/\triangle u_{\mathrm{ga}\_20}$ is 0.4375, which is also basically consistent with the result in Fig. 6(c). The abovementioned analysis results show that the complete HSS model of GCI considering the impact of digitization proposed in this article is accurate.

b) Characteristic Analysis Based on Pole Map: In this part and Section V-B2b, the poles are calculated from the closed-loop HTF shown in (33). Therefore, the stability analysis in these two sections belongs to BIBO stability analysis, that is, external stability analysis.

Under the system parameters shown in Table I, the pole maps between the reference and each output harmonic are shown in Fig. 8. From Fig. 8(a), there are five groups of poles in the system based on HSS model without considering digitization impact. Among them, the red marks are the central poles, namely, the poles corresponding to the transfer function between the reference signal and the output current of the same frequency, also namely, the poles obtained based on SSAV model. The other poles are symmetrical about the central poles, they are the poles corresponding to the transfer function between other current components and the reference signal. Obviously, all poles are on the left half plane, indicating that the system is stable. Fig. 8(b) is the pole map obtained from the complete HSS model proposed in this article. It can be seen, after considering the impact of digitization, a group of poles close to the imaginary axis is introduced into the system. This group

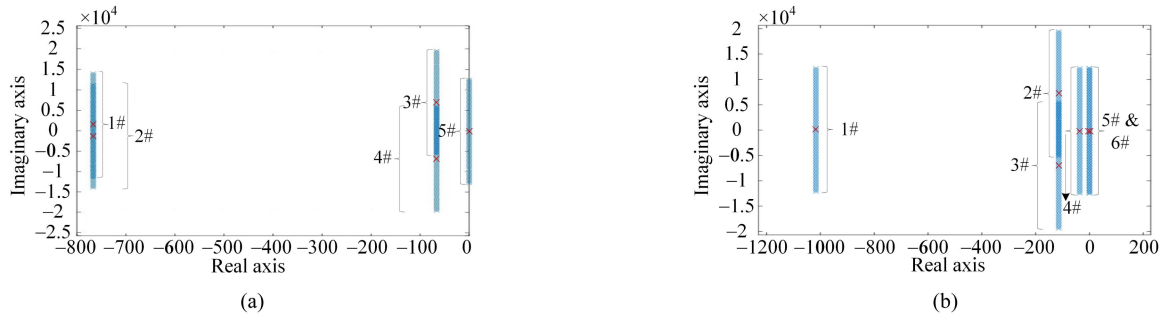

Fig. 8. Pole maps. (a) Based on HSS model without considering digitization impact. (b) Based on HSS model considering digitization impact.

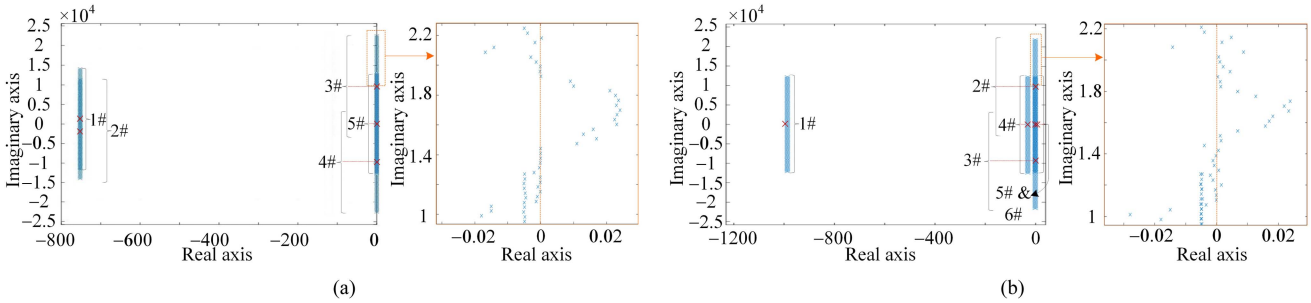

Fig. 9. Pole maps when k_p is increased to 2.7. (a) Based on HSS model without considering digitization impact. (b) Based on HSS model considering digitization impact.

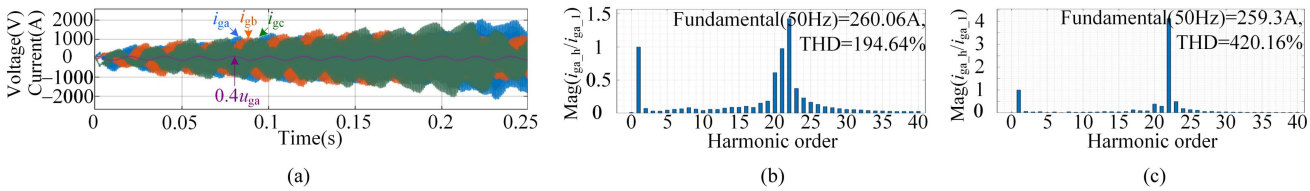

Fig. 10. Simulink circuit simulation waveforms and current spectrums when k_p is increased to 2.7. (a) Waveforms. (b) Spectrum at 0.05 s. (c) Spectrum at 0.14 s.

of poles affects the stability and output characteristics of the system, but Fig. 8(b) still shows that the system is stable. The analysis result is consistent with the circuit simulation result in Fig. 7(a).

When k_p increases to 2.7, the pole maps between the reference and each-frequency output component are shown in Fig. 9. The corresponding circuit simulation waveforms and current spectrums are shown in Fig. 10. First, it can be seen from Fig. 10, the output current of the inverter is divergent. From spectrums at 0.05 s and 0.14 s, the fundamental current is stable, but the harmonics more than 15th diverge rapidly. Next, the pole maps shown in Fig. 9 are analyzed. From Fig. 9(a), in the pole map obtained without considering the impact of digitization, the central poles are located in the left half plane, that is, the poles of the inverter system based on the SSAV model are located in the left half plane. This shows that the fundamental output is stable, which is consistent with the phenomenon reflected in Fig. 10. By observing the other poles in Fig. 9(a), the 15th–28th poles in the third group of poles are located in the right half plane, indicating that these output harmonics are unstable. This analysis result has been able to reflect some harmonic characteristics in Fig. 10, but it is still not comprehensive. Finally, Fig. 9(b) is analyzed. After considering the impact of digitization, all central poles are still located in the left half plane, indicating that the fundamental output is still stable, which is consistent with the phenomenon in Fig. 10. By observing the other poles in Fig. 9(b), the 16th–37th poles in the second group of poles are located in the right half plane, so these output harmonics are unstable. This analysis result is highly consistent with harmonic characteristic in Fig. 10.

The following conclusions can be obtained from the comparative analysis of Figs. 9 and 10. First, the SSAV model can only reflect the characteristics of the output component with the same frequency as the reference, but cannot reflect the harmonic characteristics of the system. Therefore, using SSAV model to analyze system characteristics is not comprehensive. Especially for the system with harmonic instability such as Fig. 10, the analysis results based on SSAV model deviate from the actual

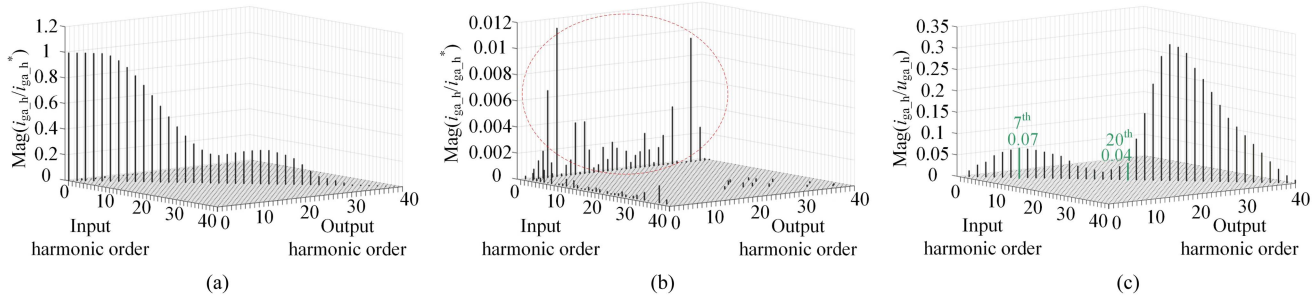

Fig. 11. Harmonic gain diagrams of GCI considering the impact of digitization. (a) Uncoupled term of i_{ga}/i_{ga}^*. (b) Coupled term of i_{ga}/i_{ga}^*. (c) i_{ga}/u_{ga}.

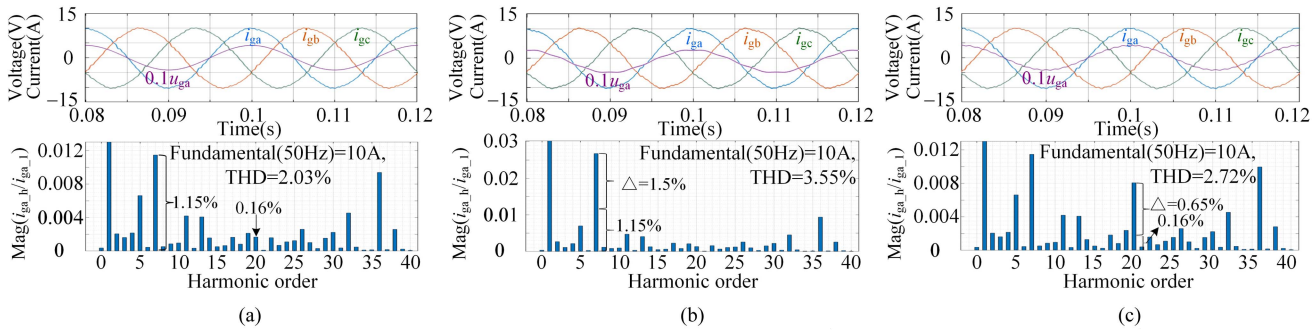

Fig. 12. Simulink circuit simulation waveforms and spectrums. (a) Under ideal grid. (b) Inject 5% seventh harmonic into grid. (c) Inject 4% 20th harmonic into grid.

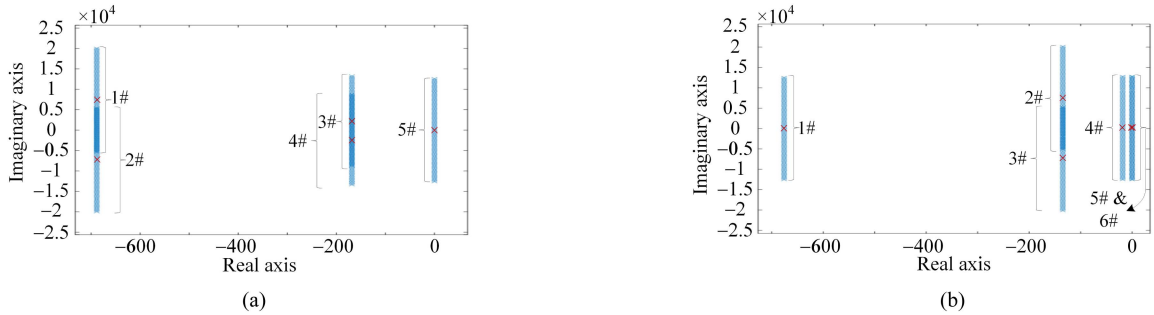

Fig. 13. Pole maps. (a) Based on HSS model without considering digitization impact. (b) Based on HSS model considering digitization impact.

system characteristics. Second, compared with the SSAV model, the HSS model can reflect the harmonic characteristics of each output component. Third, in the LSF GCI system, the impact of digitization cannot be ignored. Thus, it is necessary to consider the impact of digitization in order to further improve the accuracy of the HSS model. Fourth, the complete HSS model of GCI considering the impact of digitization proposed in this article has high accuracy.

2) Frequency-Domain Analysis Under System Parameter II: The frequency-domain analysis method of GCI under system parameter II is similar to that under system parameter I. Therefore, the frequency-domain analysis under system parameter II will be briefly described as follows.

a) Characteristic Analysis Based on Harmonic Gain Diagram: Fig. 11(a) and (b) is the harmonic gain diagrams between the input and output of the same frequency of $i_{ga}/i_{ga}{}^*$, and the harmonic gain diagram between the input and output of different frequencies of $i_{ga}/i_{ga}{}^*$, respectively. Fig. 11(a) reflects the uncoupled information of the GCI system. It can be seen that the gain between the input and output components of the same frequency attenuates to 0.7 at the tenth harmonic, indicating that the control bandwidth of the system is about 500 Hz. Fig. 11(b) reflects the coupling information of the system. The relationship between the reference and each-frequency output is focused on by this article. Fig. 11(c) shows the harmonic gain diagram of i_{ga}/u_{ga}. It is obvious that the grid harmonics will only affect the current components with the same frequency in that phase. The accuracy of Fig. 11 will be verified by the circuit simulation results as follows.

Fig. 12 shows the Simulink simulation waveforms and spectrums of grid-side current. Under the ideal grid, the spectrum data in Fig. 12(a) and that in the red box of Fig. 11(b) are

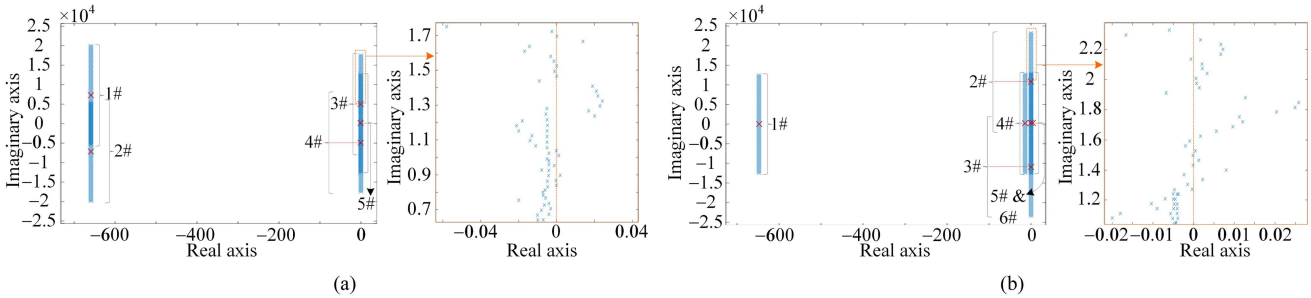

Fig. 14. Pole maps when k_p is increased to 10. (a) Based on HSS model without considering digitization impact. (b) Based on HSS model considering digitization impact.

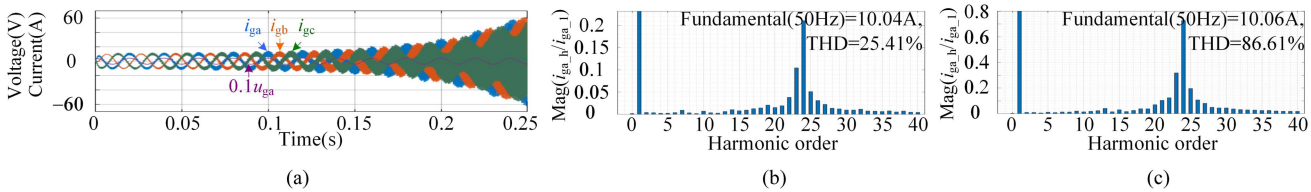

Fig. 15. Simulink circuit simulation waveforms and current spectrums when k_p is increased to 10. (a) Waveforms. (b) Spectrum at 0.05 s. (c) Spectrum at 0.14 s.

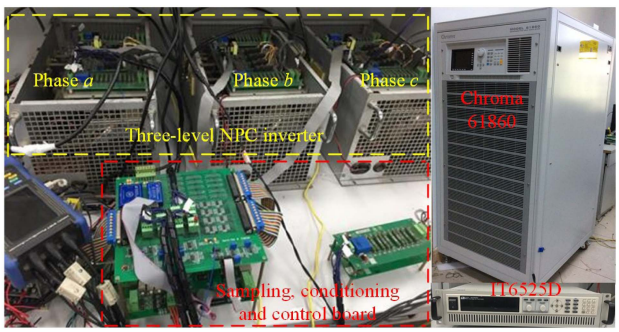

Fig. 16. Experimental platform.

basically consistent. This indicates that the HSS model considering the impact of digitization proposed in this article can accurately reflect the relationship between the reference and each output component. Similar to Section V-B1, in the small power system, the necessity of HSS modeling for LSF GCI is explained. When $f_{sw} = 2$ kHz, the sideband harmonics below the switching frequency are 18th, 20th, 24th, 26th, 30th, 32nd, 36th, and 38th harmonics. If there is no harmonic coupling, the ratio of the abovementioned sideband harmonics to the fundamental current can be obtained by double Fourier series (see [35, eqs. (7)–(9)]) as follows: 0.0003, 0.0003, 0.0057, 0.0005, 0.0003, 0.0003, 0.0009, and 0.0033. However, from Figs. 12(a) and 11(b), the ratio of the abovementioned sideband harmonics to the fundamental current is actually: 0.0008, 0.0017, 0.0011, 0.0026, 0.0022, 0.0046, 0.0094, and 0.0026. Obviously, due to the harmonic coupling in the actual GCI system, the series decomposition results corresponding to 20th, 24th, 26th, 30th, 32nd, and 36th harmonics are quite different from the actual data. Therefore, it is difficult to reflect the amplitude of sideband harmonics below the switching frequency by using double Fourier series under LSF. The HSS model is needed to analyze the output harmonic characteristics of the inverter. The abovementioned phenomenon proves the correctness of the theoretical analysis in Section II-B and is consistent with the analysis results in Section V-B1a.

Fig. 12(b) and (c), respectively, shows the output waveforms and current spectrums after injecting 5% seventh harmonic ($u_{g\_7\_peak} = 2.1$ V) and 4% 20th harmonic ($u_{g\_20\_peak} = 1.68$ V) into the grid. After 5% of the seventh harmonic is injected in the grid, the seventh harmonic in the grid-side current increases by 1.5%, so $\triangle i_{ga\_7}/\triangle u_{ga\_7}$ is 0.071. After 4% of the 20th harmonic is injected in the grid, the 20th harmonic in the grid-side current increases by 0.65%, so $\triangle i_{ga\_20}/\triangle u_{ga\_20}$ is 0.039. The above data are basically consistent with the analytical result in Fig. 11(c). The abovementioned analysis indicates that the complete HSS model considering the impact of digitization proposed in this article is accurate.

b) Characteristic Analysis Based on Pole Map: Under the system parameters shown in Table II, the pole maps between the reference and each-frequency output harmonic are shown in Fig. 13. From Fig. 13(a), when the impact of digitization is not considered, all poles of the system are on the left half plane, indicating that the system is stable. When adopting the complete HSS model considering the impact of digitization proposed in this article, it can be seen from Fig. 13(b), the consideration of digitization makes the system have an additional set of poles close to the imaginary axis. Although the consideration of digitization has a great impact on the stability and output characteristics of the system, the pole map shows that the system is still stable. This is consistent with the result of the circuit simulation in Fig. 12(a).

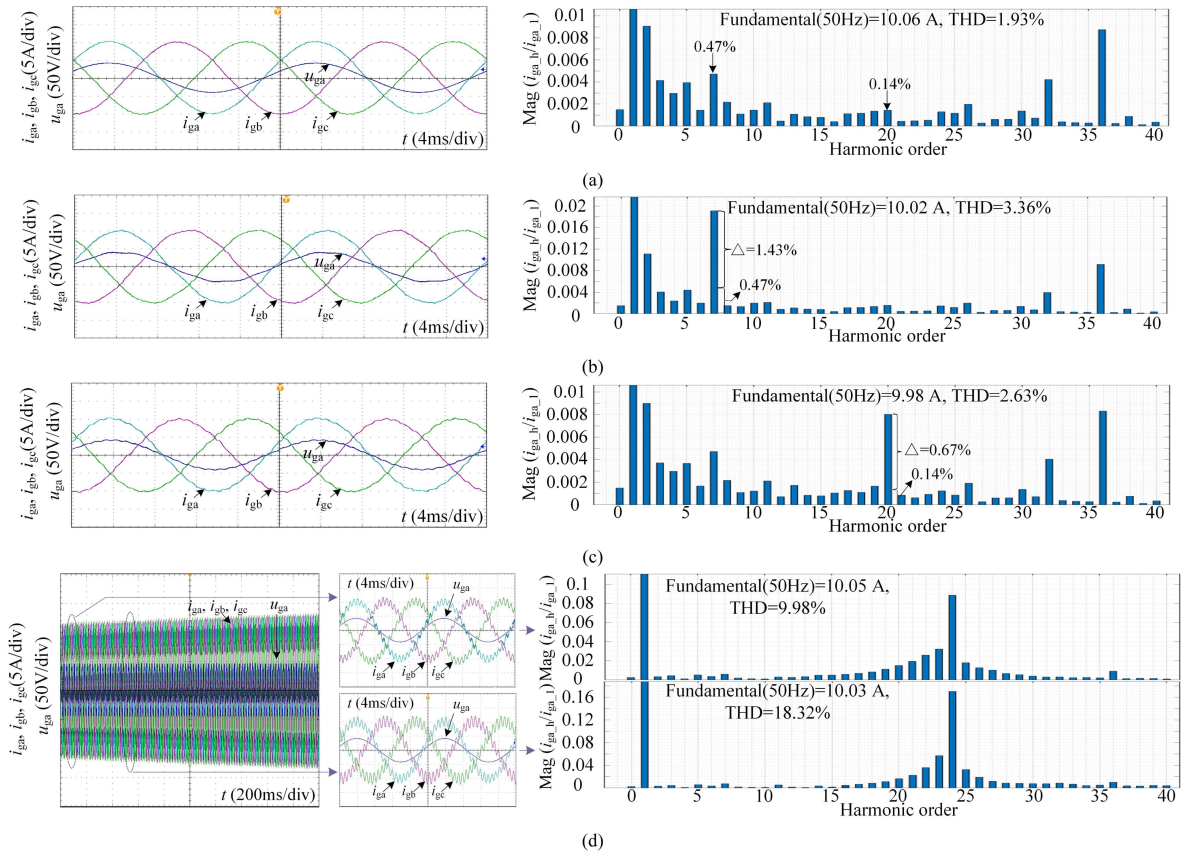

Fig. 17. Experimental waveforms and current spectrums. (a) Under ideal grid. (b) Inject 5% seventh harmonic into grid. (c) Inject 4% 20th harmonic into grid. (d) k_p is increased to 5.

When k_p increases to 10, the pole maps between the reference and each-frequency output component are shown in Fig. 14, and the corresponding circuit simulation waveforms and current spectrums are shown in Fig. 15. First, observing Fig. 15, the output current of the inverter is divergent. From the spectrums at 0.05 s and 0.14 s, it can be seen that the fundamental output is stable, while the harmonics of more than 15th diverge rapidly. Then, analyzing the pole maps shown in Fig. 14. From Fig. 14(a), in the pole map obtained without considering the impact of digitization, the central poles are located in the left half plane, that is, the poles of the inverter system based on SSAV model are located in the left half plane. This indicates that the fundamental output is stable, which is consistent with the phenomenon in Fig. 15. However, it is difficult to fully reflect the actual harmonic characteristics of the system only by the central poles. As can be seen from the other poles in Fig. 14(a), the 21st–27th poles in the third group of poles are located in the right half plane, indicating that these output harmonics are unstable. It is obvious that the pole map obtained by the HSS model without considering the digitization still cannot fully reflect the harmonic characteristics of the system. Fig. 14(b) shows the pole map obtained after considering the impact of digitization. We can find that all central poles are still located in the left half plane, so the fundamental output is still stable. From the other poles in Fig. 14(b), the 17th–37th poles in the second group of poles are located in the right half plane, indicating that these output harmonics are unstable, which is highly consistent with the harmonic characteristics in Fig. 15. According to the abovementioned comparative analysis, we can get the same conclusion as Section V-B1b, which will be briefly described as follows. For the system with stable fundamental output and unstable harmonic outputs like Fig. 15, it is not comprehensive to analyze the system characteristics by the SSAV model, the analysis results are deviated from the actual system characteristics. In addition, in the LSF GCI system, it is necessary to consider the impact of digitization, to improve the accuracy of HSS model. Finally, by comparing Figs. 14(b) and 15, the complete HSS model of GCI considering digitization impact proposed in this article has high accuracy.

VI. Experimental Verification

The experimental platform of *LCL* TL-NPC GCI based on GCF PI + CCF AD control strategy is built, to further verify the accuracy and effectiveness of the proposed model and method. In the experiment, the dc-bus voltage is supplied to the inverter through the dc power supply IT6525D, and the Chroma 61860 programmable ac power supply is used to simulate the grid. In addition, the TL phase disposition PWM is adopted, and PWM signal is generated by FPGA of XC6SLX25 produced by Xilinx. The closed-loop control, AD, sampling, protection, and other functions are all realized by TMS320C28346. The experimental parameters are shown in Table II, the switching frequency is 2 kHz, and the experimental platform is shown in Fig. 16. In order to verify the analytical results more intuitively, the experimental verification process in this section is the same as the simulation verification process in Section V-B2.

Inverter output waveforms and spectrums of i_{ga} within 2 kHz are shown in Fig. 17. First, the grid connection experiment is carried out under the ideal grid. As can be seen from Fig. 17(a), the three-phase current at the grid side is balanced, the sinusoidal degree is good, and the reference of 10 A is fully tracked. Due to nonideal factors in the experiment, there are some differences between the grid-side current spectrum in Figs. 17(a) and 11(b). However, the analytical results in Fig. 11(b) can roughly reflect the harmonic characteristics of GCI system in the experiment.

Second, injecting 5% seventh harmonic and 4% 20th harmonic into the grid, respectively. The corresponding inverter output waveforms and spectrums are shown in Fig. 17(b) and (c). It can be seen from Fig. 17(b), after 5% of the seventh harmonic is injected into the grid, the seventh harmonic in the grid-side current increases by 1.43%. So $\triangle i_{\mathrm{ga\_7}}/\triangle u_{\mathrm{ga\_7}}$ is 0.068. After 4% of the 20th harmonic is injected into the grid, the 20th harmonic increases by 0.67%. So $\triangle i_{\mathrm{ga\_20}}/\triangle u_{\mathrm{ga\_20}}$ is 0.04. The abovementioned results are basically consistent with the analytical results in Fig. 11(c).

Finally, increase k_p appropriately, observe and analyze the experimental phenomena. If k_p is too large, it will quickly trigger the overcurrent protection of the experimental platform, and it is difficult to capture the experimental waveforms.

Therefore, k_p will be increased from 1.5 to 5 in the experiment. When k_p is increased to 5, the experimental waveforms and grid-side current spectrums are shown in Fig. 17(d). It is obvious that there is divergence in the system, but it can be seen from the current spectrums that the fundamental current is always 10 A. This indicates that the fundamental component of grid-side current is stable, but some harmonic components in the grid-side current are unstable. Then, further observation of the spectrums obtained from the experiment shows that the 15th–30th harmonics diverge significantly. Here, it should be noted that when k_p exceeds a certain critical value, the value of k_p will mainly affect the divergence speed of the output component. Therefore, we can think that the experimental phenomenon in Fig. 17(d) is roughly consistent with the numerical analysis result in Fig. 14(b).

Based on the simulation results in Section V-B2 and the experimental results in this section, it can be seen, the complete HSS model of inverter considering digitization impact proposed in this article is accurate. It is not only highly consistent with the circuit simulation results, but also can basically reflect the harmonic characteristics of actual GCI system. This also indirectly shows that it is necessary to integrate the digitization impact into the HSS model or its calculation analysis process under low switching frequency.

VII. Conclusion

The calculation and analysis methods of HSS model for different applications are studied in this article, and the methods of considering the impact of digitization are proposed, respectively. According to the proposed model and method, the output harmonic characteristics of the inverter are analyzed. Finally, the accuracy of the proposed HSS-model calculation and analysis methods considering the digitization impact are verified by simulation and experiment. The results show that the proposed iterative-calculation-method of HSS model considering digitization impact and switching frequency is effective, and the proposed complete-HSS-model of GCI considering digitization impact is accurate. At the same time, it is necessary to integrate the digitization impact into HSS model or its calculation and analysis process, which can further improve the accuracy of harmonic characteristic analysis of inverter.

Appendix

$$A_i(t)=\begin{bmatrix} Z_{3\times3} & Z_{3\times3} & M_1 & M_2 \\ Z_{3\times3} & Z_{3\times3} & M_3 & Z_{3\times1} \\ M_4 & -M_4 & Z_{3\times3} & Z_{3\times1} \\ M_5 & Z_{1\times3} & Z_{1\times3} & -1/(R_{\mathrm{dc}}C_{\mathrm{dc}}) \end{bmatrix}$$

$$B_i(t)=\begin{bmatrix} M_6 & Z_{3\times3} \\ Z_{3\times3} & -M_3 \\ Z_{3\times3} & Z_{3\times3} \\ M_7 & Z_{1\times3} \end{bmatrix}, \qquad C_i(t)=\begin{bmatrix} Z_{3\times3} & I_3 & Z_{3\times4} \end{bmatrix} \tag{A1}$$

$$\begin{aligned} E_i(t)&=Z_{2\times2} \\ F_i(t)&=\begin{bmatrix} I_2 & Z_{2\times2} & -I_2 \end{bmatrix} T_{pm3}T_{cm3} \\ G_i(t)&=T_{ic}T_{ip}(k_iI_2) \\ H_i(t)&=T_{ic}T_{ip}\begin{bmatrix} k_pI_2 & -k_cI_2 & (-k_p+k_i)I_2 \end{bmatrix} T_{pm3}T_{cm3} \end{aligned} \tag{A2}$$

$$\begin{aligned} I_i(t)&=-I_2/a_d, & J_i(t)&=I_2 \\ K_i(t)&=T_{ic}T_{ip}(2I_2/a_d), & L_i(t)&=-T_{ic}T_{ip}I_2 \end{aligned} \tag{A3}$$

$$\begin{aligned} A_s(t)&=\begin{bmatrix} A(t) & Z_{10\times4} \end{bmatrix}, & B_s(t)&=B(t) \\ C_s(t)&=\begin{bmatrix} C(t) & Z_{3\times4} \end{bmatrix} \end{aligned} \tag{A4}$$

$$\begin{aligned} E_s(t)&=\begin{bmatrix} Z_{2\times2} & -I_2 & Z_{2\times7} \end{bmatrix} T_{pm4}T_{cm4} \\ F_s(t)&=\begin{bmatrix} I_2 & Z_{2\times2} \end{bmatrix} \begin{bmatrix} T_p & Z_{2\times2} \\ Z_{2\times2} & T_p \end{bmatrix} \begin{bmatrix} T_c & Z_{2\times3} \\ Z_{2\times3} & T_c \end{bmatrix} \\ G_s(t)&= \begin{bmatrix} -k_cI_2 & (-k_p+k_c)I_2 & Z_{2\times3} & k_iI_2 & Z_{2\times3} \\ Z_{2\times2} & Z_{2\times2} & Z_{2\times3} & Z_{2\times2} & Z_{2\times2} \end{bmatrix} T_{pm4}T_{cm4} \\ H_s(t)&=\begin{bmatrix} k_pI_2 & Z_{2\times2} \\ Z_{2\times2} & I_2 \end{bmatrix} \begin{bmatrix} T_p & Z_{2\times2} \\ Z_{2\times2} & T_p \end{bmatrix} \begin{bmatrix} T_c & Z_{2\times3} \\ Z_{2\times3} & T_c \end{bmatrix} \end{aligned} \tag{A5}$$

$$\begin{aligned} I_s(t)&=\begin{bmatrix} Z_{1\times9} & -1/a & 0 \\ Z_{1\times9} & 0 & 1/a \end{bmatrix} T_{pm4}T_{cm4},\ J_s(t)=\begin{bmatrix} I_2 & Z_{2\times2} \end{bmatrix} \\ K_s(t)&= \begin{bmatrix} T_{ic} & Z_{3\times2} \\ Z_{3\times2} & T_{ic} \end{bmatrix} \begin{bmatrix} T_{ip} & Z_{2\times2} \\ Z_{2\times2} & T_{ip} \end{bmatrix} \begin{bmatrix} Z_{2\times9} & 2I_2/a \\ Z_{2\times9} & Z_{2\times2} \end{bmatrix} T_{pm4}T_{cm4} \\ L_s(t)&=\begin{bmatrix} T_{ic} & Z_{3\times2} \\ Z_{3\times2} & T_{ic} \end{bmatrix} \begin{bmatrix} T_{ip} & Z_{2\times2} \\ Z_{2\times2} & T_{ip} \end{bmatrix} \begin{bmatrix} -I_2 & Z_{2\times2} \\ Z_{2\times2} & I_2 \end{bmatrix}. \end{aligned} \tag{A6}$$

Where in

$$M_1 = \text{diag}(\,-1/L_1\ -1/L_1\ -1/L_1\,)$$
$$M_2 = \left[\,S_a/2L_1\ S_b/2L_1\ S_c/2L_1\,\right]^{\mathrm{T}}$$
$$M_3 = \text{diag}(\,1/L_2\ 1/L_2\ 1/L_2\,)$$
$$M_4 = \text{diag}(\,1/C\ 1/C\ 1/C\,)$$
$$M_5 = \left[\,S_a/C_{\text{dc}}\ S_b/C_{\text{dc}}\ S_c/C_{\text{dc}}\,\right]$$
$$M_6 = -M_1 \cdot U_{\text{dc}}/2,$$
$$M_7 = \left[\,I_{ia}/C_{\text{dc}}\ I_{ib}/C_{\text{dc}}\ I_{ic}/C_{\text{dc}}\,\right].$$

k_p, k_i, and k_c are proportional, integral gains of PI controller, and AD coefficient, respectively. $Z_{m\times n}$ represents the $m\times n$ zero matrix, and I_e represents e dimensional identity matrix. T_p, T_c, T_{ip}, and T_{ic} represent Park transform, Clarke transform, Park inverse transform, and Clarke inverse transform, respectively. Their expressions are shown in (A7).

In addition, the frequency expressions of $\sin\theta_0$ and $\cos\theta_0$ are: $F(\sin\theta_0) = \{\ldots 0, 0, 0.5j, 0, -0.5j, 0, 0, \ldots\}$, $F(\cos\theta_0) = \{\ldots 0, 0, 0.5, 0, 0.5, 0, 0, \ldots\}$. In the HSS model, the frequency expressions of $\sin\theta_0$ and $\cos\theta_0$ need to be expressed in the form of Toeplitz matrix

$$T_c = \begin{bmatrix} 2/3 & -1/3 & -1/3 \\ 0 & 1/\sqrt{3} & -1/\sqrt{3} \end{bmatrix}, \quad T_p = \begin{bmatrix} \cos\theta_0 & \sin\theta_0 \\ -\sin\theta_0 & \cos\theta_0 \end{bmatrix}$$

$$T_{ic} = \begin{bmatrix} 1 & -1/2 & -1/2 \\ 0 & \sqrt{3}/2 & -\sqrt{3}/2 \end{bmatrix}^{\mathrm{T}}, \quad T_{ip} = \begin{bmatrix} \cos\theta_0 & -\sin\theta_0 \\ \sin\theta_0 & \cos\theta_0 \end{bmatrix}$$

$$T_{pm3} = \begin{bmatrix} T_p & Z_{2\times2} & Z_{2\times2} \\ Z_{2\times2} & T_p & Z_{2\times2} \\ Z_{2\times2} & Z_{2\times2} & T_p \end{bmatrix}, \ T_{cm3} = \begin{bmatrix} T_c & Z_{2\times3} & Z_{2\times3} \\ Z_{2\times3} & T_c & Z_{2\times3} \\ Z_{2\times3} & Z_{2\times3} & T_c \end{bmatrix}$$

$$T_{pm4} = \begin{bmatrix} T_p & Z_{2\times2} & Z_{2\times2} & Z_{2\times5} \\ Z_{2\times2} & T_p & Z_{2\times2} & Z_{2\times5} \\ Z_{2\times2} & Z_{2\times2} & T_p & Z_{2\times5} \\ Z_{5\times2} & Z_{5\times2} & Z_{5\times2} & I_5 \end{bmatrix}$$

$$T_{cm4} = \begin{bmatrix} T_c & Z_{2\times3} & Z_{2\times3} & Z_{2\times5} \\ Z_{2\times3} & T_c & Z_{2\times3} & Z_{2\times5} \\ Z_{2\times3} & Z_{2\times3} & T_c & Z_{2\times5} \\ Z_{5\times3} & Z_{5\times3} & Z_{5\times3} & I_5 \end{bmatrix}. \tag{A7}$$

REFERENCES

[1] X. Wang and F. Blaabjerg, "Harmonic stability in power electronic-based power systems: Concept, modeling, and analysis," *IEEE Trans. Smart Grid*, vol. 10, no. 3, pp. 2858–2870, May 2019.

[2] T. Liu, J. Liu, Z. Liu, and Z. Liu, "A study of virtual resistor-based active damping alternatives for LCL resonance in grid-connected voltage source inverters," *IEEE Trans. Power Electron.*, vol. 35, no. 1, pp. 247–262, Jan. 2020.

[3] Y. Xuan, M. Tian, X. Song, W. Chen, and X. Yang, "Design and implementation of a high power three-level T-type inverter for a photovoltaic system," in *Proc. 9th Int. Conf. Power Electron. ECCE Asia*, 2015, pp. 2808–2813.

[4] X. Xiao, N. Xie, Y. Zhou, X. Liu, and W. Zhao, "Study on high voltage grid-connected PV inverter based on modular multilevel converter," in *Proc. Int. Conf. Power Syst. Technol.*, 2018, pp. 1295–1299.

[5] X. Zhang, J. W. Spencer, and J. M. Guerrero, "Small-signal modeling of digitally controlled grid-connected inverters with LCL filters," *IEEE Trans. Ind. Electron.*, vol. 60, no. 9, pp. 3752–3765, Sep. 2013.

[6] B. Hoff and W. Sulkowski, "Grid-connected VSI with LCL filter—Models and comparison," *IEEE Trans. Ind. Appl.*, vol. 50, no. 3, pp. 1974–1981, May/Jun. 2014.

[7] J. Sun, "Small-signal methods for AC distributed power systems—A review," *IEEE Trans. Power Electron.*, vol. 24, no. 11, pp. 2545–2554, Nov. 2009.

[8] A. Tahavorgar and J. E. Quaicoe, "Stability and small-signal analyses of the dual series-resonant DC–DC converter," *IEEE Trans. Power Electron.*, vol. 34, no. 2, pp. 1420–1430, Feb. 2019.

[9] S. Golestan, J. M. Guerrero, J. C. Vasquez, A. M. Abusorrah, and Y. Al-Turki, "Harmonic linearization and investigation of three-phase parallel-structured signal decomposition algorithms in grid-connected applications," *IEEE Trans. Power Electron.*, vol. 36, no. 4, pp. 4198–4213, Apr. 2021.

[10] Ö. C. Sakinci and J. Beerten, "Generalized dynamic phasor modeling of the MMC for small-signal stability analysis," *IEEE Trans. Power Del.*, vol. 34, no. 3, pp. 991–1000, Jun. 2019.

[11] A. Bagheri, M. Mardaneh, A. Rajaei, and A. Rahideh, "Detection of grid voltage fundamental and harmonic components using Kalman filter and generalized averaging method," *IEEE Trans. Power Electron.*, vol. 31, no. 2, pp. 1064–1073, Feb. 2016.

[12] M. Daryabak et al., "Modeling of LCC-HVDC systems using dynamic phasors," *IEEE Trans. Power Del.*, vol. 29, no. 4, pp. 1989–1998, Aug. 2014.

[13] Z. Shuai, Y. Peng, J. M. Guerrero, Y. Li, and Z. J. Shen, "Transient response analysis of inverter-based microgrids under unbalanced conditions using a dynamic phasor model," *IEEE Trans. Ind. Electron.*, vol. 66, no. 4, pp. 2868–2879, Apr. 2019.

[14] D. Venkatramanan and V. John, "Dynamic phasor modeling and stability analysis of SRF-PLL-based grid-tie inverter under islanded conditions," *IEEE Trans. Ind. Appl.*, vol. 56, no. 2, pp. 1953–1965, Mar./Apr. 2020.

[15] J. A. Mueller and J. W. Kimball, "An improved generalized average model of DC–DC dual active bridge converters," *IEEE Trans. Power Electron.*, vol. 33, no. 11, pp. 9975–9988, Nov. 2018.

[16] J. R. C. Orillaza and A. R. Wood, "Harmonic state-space model of a controlled TCR," *IEEE Trans. Power Del.*, vol. 28, no. 1, pp. 197–205, Jan. 2013.

[17] X. Yue, X. Wang, and F. Blaabjerg, "Review of small-signal modeling methods including frequency-coupling dynamics of power converters," *IEEE Trans. Power Electron.*, vol. 34, no. 4, pp. 3313–3328, Apr. 2019.

[18] J. Kwon, X. Wang, F. Blaabjerg, C. L. Bak, A. R. Wood, and N. R. Watson, "Linearized modeling methods of AC–DC converters for an accurate frequency response," *IEEE J. Emerg. Sel. Topics Power Electron.*, vol. 5, no. 4, pp. 1526–1541, Dec. 2017.

[19] Z. Xu, B. Li, S. Wang, S. Zhang, and D. Xu, "Generalized single-phase harmonic state space modeling of the modular multilevel converter with zero-sequence voltage compensation," *IEEE Trans. Ind. Electron.*, vol. 66, no. 8, pp. 6416–6426, Aug. 2019.

[20] J. Lyu, X. Zhang, X. Cai, and M. Molinas, "Harmonic state-space based small-signal impedance modeling of a modular multilevel converter with consideration of internal harmonic dynamics," *IEEE Trans. Power Electron.*, vol. 34, no. 3, pp. 2134–2148, Mar. 2019.

[21] Z. Xu et al., "A complete HSS-based impedance model of MMC considering grid impedance coupling," *IEEE Trans. Power Electron.*, vol. 35, no. 12, pp. 12929–12948, Dec. 2020.

[22] J. Kwon, X. Wang, F. Blaabjerg, and C. L. Bak, "Frequency-domain modeling and simulation of DC power electronic systems using harmonic state space method," *IEEE Trans. Power Electron.*, vol. 32, no. 2, pp. 1044–1055, Feb. 2017.

[23] J. Kwon, X. Wang, C. L. Bak, and F. Blaabjerg, "Harmonic instability analysis of single-phase grid connected converter using harmonic state space (HSS) modeling method," in *Proc. IEEE Energy Convers. Congr. Expo.*, 2015, pp. 2421–2428.

[24] J. Kwon, X. Wang, C. L. Bak, and F. Blaabjerg, "Harmonic interaction analysis in grid connected converter using harmonic state space (HSS) modeling," in *Proc. IEEE Appl. Power Electron. Conf. Expo.*, 2015, pp. 1779–1786.

[25] J. B. Kwon, X. Wang, F. Blaabjerg, and C. L. Bak, "Precise model analysis for 3-phase high power converter using the harmonic state space modeling," in *Proc. 9th Int. Conf. Power Electron. ECCC Asia*, 2015, pp. 2628–2635.

[26] V. Salis, A. Costabeber, S. M. Cox, P. Zanchetta, and A. Formentini, "Stability boundary analysis in single-phase grid-connected inverters with PLL by LTP theory," *IEEE Trans. Power Electron.*, vol. 33, no. 5, pp. 4023–4036, May 2018.

[27] X. Chen, S. Yu, and X. Ge, "Modelling and stability analysis of virtual synchronous machine using harmonic state-space modelling method," *J. Eng.*, vol. 2019, no. 16, pp. 2597–2603, Dec. 2018.
[28] J. Kwon, X. Wang, C. L. Bak, and F. Blaabjerg, "Analysis of harmonic coupling and stability in back-to-back converter systems for wind turbines using harmonic state space (HSS)," in *Proc. IEEE Energy Convers. Congr. Expo.*, 2015, pp. 730–737.
[29] J. Kwon, X. Wang, C. L. Bak, and F. Blaabjerg, "The modeling and harmonic coupling analysis of multiple-parallel connected inverter using harmonic state space (HSS)," in *Proc. IEEE Energy Convers. Congr. Expo.*, 2015, pp. 6231–6238.
[30] C. Gong, W. K. Sou, and C. S. Lam, "H∞ optimal control design of static var compensator coupling hybrid active power filter based on harmonic state-space modeling," *CPSS Trans. Power Electron. Appl.*, vol. 6, no. 3, pp. 227–234, Sep. 2021.
[31] D. Sun, X. Lu, and L. Du, "Optimal design of grid interactive inverters based on harmonic state space modeling," in *Proc. IEEE Energy Convers. Congr. Expo.*, 2020, pp. 5040–5045.
[32] J. Zhang, L. Guo, and J. Ye, "Cyber-attack detection for photovoltaic farms based on power-electronics-enabled harmonic state space modeling," *IEEE Trans. Smart Grid*, vol. 13, no. 5, pp. 3929–3942, Sep. 2022.
[33] J. J. Rico, M. Madrigal, and E. Acha, "Dynamic harmonic evolution using the extended harmonic domain," *IEEE Trans. Power Del.*, vol. 18, no. 2, pp. 587–594, Apr. 2003.
[34] N. M. Wereley, "Analysis and control of linear periodically time varying systems," Ph.D. dissertation, Dept. Aeronaut. Astronaut., Massachusetts Inst. Technol., Cambridge, MA, USA, 1991.
[35] Y. Cai, Y. He, H. Zhou, and J. Liu, "Design method of LCL filter for grid-connected inverter based on particle swarm optimization and screening method," *IEEE Trans. Power Electron.*, vol. 36, no. 9, pp. 10097–10113, Sep. 2021.

Yuxi Cai (Student Member, IEEE) received the B.S. and M.S. degrees in electrical engineering from the Xi'an University of Technology, Xi'an, China, in 2016 and 2019, respectively. She is currently working toward the Ph.D. degree in electrical engineering with Xi'an Jiaotong University, Xi'an, China.

Her research interests focus on the application of power electronics in power system.

Yingjie He (Senior Member, IEEE) received the B.S., M.S., and Ph.D. degrees from the Huazhong University of Science and Technology, Wuhan, China, in 1999, 2003, and 2007, respectively.

He was then with the Power Electronics and Renewable Energy Center, Xi'an Jiaotong University (XJTU), Xi'an, China, as a Postdoctoral Researcher, and with Aalborg University, Aalborg, Denmark, as a Visiting Scholar. He is currently an Associate Professor and the Doctoral Supervisor with XJTU. He is selected as the High-level Talent of Shaanxi Power Supply Society and the High-level Talent of Zhenjiang, Jiangsu. He has authored or coauthored more than 100 journal and conference papers, such as IEEE TRANSACTIONS ON POWER ELECTRONICS and IEEE TRANSACTIONS ON INDUSTRIAL ELECTRONICS. His research interests include multilevel converter and its control technology, application of power electronics in power system, power quality and its control technology.

Dr. He is an Executive Director of IEEE Flexible AC Transmission Technology Subcommittee (China), Executive Director of Shaanxi Power Supply Society, Senior Member of China Electrotechnical Society, Member of Power Quality Special Committee of China Power Supply Society, and appraisal expert of National Natural Science Foundation and Ministry of Science and Technology of China. He was the recipient of the Second Prize of Science and Technology Progress from China Power Supply Society in 2021, the Science and Technology Progress Award from Shaanxi Power Supply Society in 2022, and the Special Contribution Award from Proceedings of the CSEE.

Haixiao Zhang (Student Member, IEEE) received the B.S. degree in electrical engineering from Wuhan University, Wuhan, China, in 2020. He is currently working toward the M.S. degree in electrical engineering with Xi'an Jiaotong University, Xi'an, China.

His research interests focus on the application of power electronics in power system.

Hongwei Zhou (Member, IEEE) received the B.S. and M.S. degrees in electrical engineering from the Xi'an University of Technology, Xi'an, China, in 2007 and 2010, respectively. He is currently working toward the Ph.D. degree in electrical engineering with Xi'an Jiaotong University, Xi'an, China.

His main research interests include modeling and control of PV grid-connected converters and stability of power electronic based power systems.

Jinjun Liu (Fellow, IEEE) received the B.S. and Ph.D. degrees in electrical engineering from Xi'an Jiaotong University (XJTU), Xi'an, China, in 1992 and 1997, respectively.

He was a Faculty with the School of Electrical Engineering, XJTU. From late 1999 to early 2002, he was a Visiting Scholar with the Center for Power Electronics Systems, Virginia Polytechnic Institute and State University, Blacksburg, VA, USA. In late 2002, he was promoted to a Full Professor and then the Head of the Power Electronics and Renewable Energy Center, XJTU, which now comprises more than 20 faculty members and more than 200 graduate students and carries one of the leading power electronics programs in China. From 2005 to early 2010, he was an Associate Dean with the School of Electrical Engineering, XJTU, and from 2009 to early 2015, the Dean for Undergraduate Education of XJTU. He is currently a XJTU Distinguished Professor of power electronics. He coauthored three books (including one textbook), authored or coauthored more than 500 technical papers in peer-reviewed journals and conference proceedings, holds more than 50 invention patents (China/US/Europe), and delivered for many times plenary keynote speeches and tutorials at IEEE conferences or China national conferences in power electronics area. His research interests include modeling, control, and design methods for power converters and electronified power systems, power quality control and utility applications of power electronics, and micro-grids for sustainable energy and distributed generation.

Dr. Liu was the recipient of eight times governmental awards at national level or provincial/ministerial level for scientific research/teaching achievements, 2006 Delta Scholar Award, the 2014 Chang Jiang Scholar Award, the 2014 Outstanding Sci-Tech Worker of the Nation Award, the 2016 State Council Special Subsidy Award, the IEEE TRANSACTIONS ON POWER ELECTRONICS 2016 and 2021 Prize Paper Awards, and the Nomination Award for the Grand Prize of 2020 Bao Steel Outstanding Teacher Award. He was as the IEEE Power Electronics Society Region 10 Liaison and then China Liaison for 10 years, has been an Associate Editor for IEEE TRANSACTIONS ON POWER ELECTRONICS since 2006; from 2015 to 2019, was the Executive Vice President; and from 2020 to 2021, was the Vice President for Membership of IEEE PELS. He was on the Board of China Electrotechnical Society 2012–2020 and was elected the Vice President in 2013 and the Secretary General in 2018 of the CES Power Electronics Society. Since 2013, he has been the Vice President for International Affairs, China Power Supply Society (CPSS) and since 2016, the inaugural Editor-in-Chief for CPSS Transactions on Power Electronics and Applications. Since 2013, he has been the Vice Chair of the Chinese National Steering Committee for College Electric Power Engineering Programs.